

Simulation of Phase Domain Breakup and Coalescence in Strong Shear and Transient Flows Using Lattice-Boltzmann Method

by

Akihiko Suwa

B.S. Applied Physics
Northeastern University, 1995

SUBMITTED TO THE DEPARTMENT OF MATERIALS SCIENCE AND
ENGINEERING IN PARTIAL FULFILLMENT OF THE REQUIREMENTS FOR THE
DEGREE OF

MASTER OF SCIENCE IN MATERIALS SCIENCE AND ENGINEERING
AT THE
MASSACHUSETTS INSTITUTE OF TECHNOLOGY

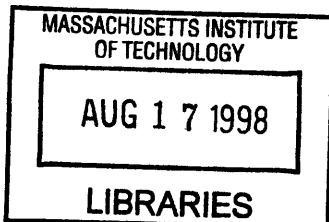
FEBRUARY 1998

© 1998 Massachusetts Institute of Technology. All rights reserved.

Signature of Author
Department of Materials Science and Engineering
January 16, 1998

Certified by
Chris E. Scott
Assistant Professor of Polymer Engineering
Thesis Supervisor

Accepted by
Linn W. Hobbs
John F. Elliott Professor of Materials
Chairman, Departmental Committee on Graduate Students



Simulation of Phase Domain Breakup and Coalescence in Strong Shear and Transient Flows Using Lattice-Boltzmann Method

by

Akihiko Suwa

Submitted to the Department of Materials Science and Engineering

on January 16, 1998 in Partial Fulfillment of the Requirements

for the Degree of Master of Science in Materials Science and Engineering

ABSTRACT

The lattice-Boltzmann method was used for three-dimensional simulation of droplet breakup and coalescence in flow fields representative of those encountered in compounding of immiscible polymer blends. Quantitative confirmation of droplet deformation in simple shear was conducted using this method, and showed very good agreement with theoretical results. Droplet breakup in simple shear was simulated quantitatively, and agreed very well with both experimental and theoretical results. Capillary wave instability and end-pinching were simulated, and showed semi-quantitative agreement with theory and experiments. Breakup and coalescence of droplets in high-dispersed phase concentration was also simulated qualitatively. Limitations inherent to the model and future modifications needed for more accurate simulation of multiphase flow are discussed.

Thesis Supervisor: Chris E. Scott
Title: Assistant Professor of Polymer Engineering

Table of Contents

1	Introduction	8
2	Cellular Automata	10
2.1	Lattice-Gas Automata	10
2.2	Lattice-Boltzmann Method	16
3	Quantitative Verification of the Lattice-Boltzmann Method	20
3.1	Simulation Setup	20
3.2	Drag Flow Between Parallel Plates with One Plate Suddenly Set in Motion	21
3.3	Pressure Flow of a Newtonian Fluid Between Parallel Plates	22
3.4	Pressure Flow of a Power-Law Fluid Between Parallel Plates	26
3.5	Steady State Sphere and Cylinder	29
3.6	Deformation of a Droplet in Simple Shear Flow	32
4	Capillary Wave Instability	35
4.1	Introduction	35
4.2	Perturbation in the Lattice-Boltzmann Method	38
4.3	Forced Perturbation	42
4.4	Examination of Limitations of the Lattice-Boltzmann Method	45

5 Applications	56
5.1 Introduction	56
5.2 Breakup in Simple Shear Flow vs. Capillary Number	61
5.3 End-pinching	65
5.4 Coalescence of a Doublet	71
5.5 Effect of Coalescence in Equilibrium of Mixing	79
6 Conclusion	84
7 Bibliography	86

List of Figures

Figure 2.1	Propagation and collision in the single-phase lattice-gas automata model .	12
Figure 2.2	$\bar{n} = (1,1,0,1,0,0)$	13
Figure 2.3	No-slip wall boundary condition	13
Figure 2.4	Propagation and collision in the two-phase lattice-gas automata model . .	15
Figure 2.5	Creating interfacial tension	16
Figure 3.1	Velocity profile of drag flow between parallel plates	21
Figure 3.2	Velocity profile of pressure flow between parallel plates of a Newtonian fluid	23
Figure 3.3	Correction to the virtual wall boundary location	25
Figure 3.4	Linear relationship between $v_{x,max}$ and $\Delta P/L$	25
Figure 3.5	Linear relationship between $v_{x,max}$ and $1/\eta$	26
Figure 3.6	Velocity profile of pressure flow between parallel plates of a power law fluid with a power law index of 1.5	28
Figure 3.7	Velocity profile of pressure flow between parallel plates of a power law fluid with a power law index of 0.6	28
Figure 3.8	Linear relationship between interfacial tension and A	30
Figure 3.9	Linear relationship between interfacial tension and f	31
Figure 3.10	Linear relationship between interfacial tension and $-1/\delta$	31
Figure 3.11	Nomenclature for deformation of a droplet in simple shear	33
Figure 3.12	Lattice-Boltzmann rendering of deformation of a droplet in simple shear	33
Figure 3.13	Deformation vs. initial capillary number	34
Figure 4.1	Lattice-Boltzmann rendering of capillary wave instability	35
Figure 4.2	Nomenclature for the capillary wave disturbance	36
Figure 4.3	Fastest growing wavelength vs. viscosity ratio	36
Figure 4.4	Growth rate vs. X at $\eta=1$	38
Figure 4.5	Mass- and momentum-conserving perturbation in the lattice-Boltzmann method	40
Figure 4.6	Propagation of a transverse wave via propagation of a longitudinal wave .	44
Figure 4.7	Amplitude of a discrete perturbation	46
Figure 4.8	Discretization of the wave growth	47
Figure 4.9	Shape-capitalization of the fastest growing wave	48
Figure 4.10	Potential shape-capitalizing wavelengths at $t_b=2,000$	50

Figure 4.11	Potential shape-capitalizing wavelengths at $t_b=20,000$	51
Figure 4.12	Potential shape-capitalizing wavelengths at $t_b=200,000$	51
Figure 4.13	Effect of increasing the thread diameter in narrowing the range of shape capitalizing wavelengths	53
Figure 4.14	Effect of the large perturbation amplitude in the growth rate	54
Figure 4.15	Shift in the fastest growing wavelength due to the large perturbation amplitude	55
Figure 5.1	Four-roller device.	57
Figure 5.2	Critical capillary number vs. viscosity ratio at different flow profiles . . .	58
Figure 5.3	Three modes of collision	60
Figure 5.4	Continuous elongation of a droplet at the critical capillary number	62
Figure 5.5	Shapes of the droplet at breakup in simple shear flow	63
Figure 5.6	Critical capillary number vs. viscosity ratio in simple shear	64
Figure 5.7	Velocity profile of a deformed droplet in simple shear	65
Figure 5.8	Definition of degree of elongation	66
Figure 5.9	Elongated droplet shapes at different viscosity ratios	66
Figure 5.10	End-pinching and coalescence as functions of L/a and viscosity ratio . .	67
Figure 5.11	Comparison of time for end-pinching and coalescence in experiment and simulations	69
Figure 5.12	Velocity profile of a droplet for end-pinching and coalescence	70
Figure 5.13	Incorrect interface recognition in the lattice-Boltzmann method	72
Figure 5.14	Coalescence/bounce of doublet vs. phase angle	74
Figure 5.15	Color pair	75
Figure 5.16	Condition for two interfaces occurring at a single lattice point	76
Figure 5.17	Limitation of color re-distribution due to lattice	77
Figure 5.18	Delay in coalescence by improvement in color separation	78
Figure 5.19	Equilibrium droplet diameter vs. dispersed phase concentration: experiment.	79
Figure 5.20	Typical states of mixing equilibrium simulated by the lattice-Boltzmann method at different dispersed phase concentrations	81
Figure 5.21	Equilibrium droplet diameter vs. dispersed phase concentration: the lattice-Boltzmann method.	82

List of Tables

Table 4.1 Fastest growing wavelengths and growth rates of capillary wave instability using difference perturbation methods	41
Table 4.2 Fastest growing wavelengths and growth rates of capillary wave instability using forced perturbation scheme	45

1. Introduction

Characteristics exhibited by a single polymer are often insufficient to satisfy requirements demanded by today's applications. In polymer processing, single-screw, and twin screw extruders and batch mixers are used to blend different polymers to achieve these optimal, desired product characteristics. The breakup and coalescence of fluid droplets in processing is important since these processes often determine the product morphology. For example, when a rubber is dispersed in a nylon matrix, the impact strength of the blend jumps up nearly an order of magnitude as the rubber particle diameter drops below 0.5 - 2 μm [1].

Most experimental polymer blends are first created in lab-size batch mixers and extruders. In commercial production, larger commercial-size extruders and batch mixers are used for mixing. Since a larger extruder does not mix the materials in same way as a smaller one does, the scalability of mixing becomes a crucial issue in production. Currently, obtaining the same morphology achieved by a lab-sized extruder using a commercial extruder is done on a trial-and-error basis. Even if it results in success, this trial and error process is still very time-consuming, cost-inefficient and generates significant waste.

To avoid such a time-consuming and wasteful process, an effective modeling technique that can accurately simulate the breakup and coalescence of immiscible polymer particles in a batch mixer and an extruder is required. Challenges associated with modeling of these processes include simulation of: high-dispersed phase concentrations, complex

boundary conditions, moving phase boundaries, and non-Newtonian rheology of these multiphase flows.

The simulation techniques most widely used for modeling polymer blending today are the finite element method and its variations. However, these methods have difficulties in answering the challenges described above.

In this thesis, the author looks into a computational fluid dynamics (CFD) model called the lattice-Boltzmann method and evaluates whether this approach to CFD can provide solutions to the challenges described above. The author will begin by describing lattice-gas automata, a model that precedes the lattice-Boltzmann method, and then describe, benchmark, and apply the lattice-Boltzmann method.

2. Cellular Automata

2.1 Lattice-gas Automata

A two-dimensional fluid model called the HPP model, using a square lattice and fictitious particles of discrete mass, velocity and time step was first introduced in 1973 [2]. Because it is entirely discrete, and because the evolution at each site is determined by the state of the site and its nearest neighbors, a model of this nature is defined as a cellular automaton or lattice-gas automata [3]. This model, however, has serious omissions such as lack of Galilean invariance and lack of isotropy, which are necessary for simulating fluid dynamics [4].

In 1986, a new model that overcomes the above discrepancies and that simulates the Navier-Stokes equation was introduced by Frisch, Hasslacher and Pomeau [5] and is called the FHP model. In their model, at microscopic scale, particles of unit mass with unit velocity propagate on a triangular lattice and meet at lattice sites, colliding with each other such that mass and momentum are locally conserved, as shown in Figure 2-1. Microdynamical equations of mass and momentum conservation for the lattice-gas model are given below [6].

$$\sum_i n_i(\bar{x} + \bar{c}_i, t + 1) = \sum_i n_i(\bar{x}, t) \quad (2-1)$$

$$\sum_i \bar{c}_i n_i(\bar{x} + \bar{c}_i, t + 1) = \sum_i \bar{c}_i n_i(\bar{x}, t) \quad (2-2)$$

Here $n_i(\bar{x}, t) = 1$ if a particle is present and is moving in i th direction at the lattice location \bar{x} at time t , and $n_i(\bar{x}, t) = 0$ if a particle is absent. \bar{c}_i is the unit lattice vector in i th direction. The equation of evolution is given by:

$$n_i(\bar{x} + \bar{c}_i, t + 1) = n_i(\bar{x}, t) + \Delta_i[\bar{n}_i(\bar{x}, t)] \quad (2-3)$$

where Δ_i is a collision operator with values of 1, 0 or -1, and $\bar{n}_i = (n_1, n_2, n_3, n_4, n_5, n_6)$ for the 2-D FHP model as shown in Figure 2-2. The collision operators Δ_i are different for each model. For example, the operator for the three-body collision shown in Figure 2-1 is given by

$$\Delta_i^{(3)} = n_{i+1}n_{i+3}n_{i+5}\bar{n}_i\bar{n}_{i+2}\bar{n}_{i+4} - \bar{n}_{i+1}\bar{n}_{i+3}\bar{n}_{i+5}n_in_{i+2}n_{i+4} \quad (2-4)$$

where $\bar{n}_i = 1 - n_i$.

At the macroscopic scale, or when enough time or spatial averaging is used, the collective behavior of the particles becomes analogous to that of incompressible Navier-Stokes flow. Along with the Boltzmann approximation and the small velocity assumption, the incompressible Navier-Stokes equation can be derived analytically starting from equations (2-1), (2-2), and (2-3) [7]. The analytical derivation of the Navier-Stokes equation from microscopic lattice-gas hydrodynamics is discussed in detail by Rothman [6]. In the FHP model, the pressure of the fluid is decided by the density of the particles, and the viscosity of the fluid is determined by the collision rules and the density. The validity of the FHP model for simulating fluid dynamics has been tested by many authors [6].

One of unique characteristics of the FHP model is its straight-forward implementation of the no-slip boundary condition as shown in Figure 2-3. When a particle

arrives at a “solid wall” lattice point, it is simply bounced back to the direction it came. When this so-called no-slip boundary condition is used, an effective boundary between the fluid and the wall is created approximately halfway between the lattice point where the average velocity is zero. This ease of boundary condition implementation allows the FHP model to analyze complex boundary problems such as flow through porous media [8], which are otherwise very difficult to simulate using conventional computational fluid dynamics techniques.

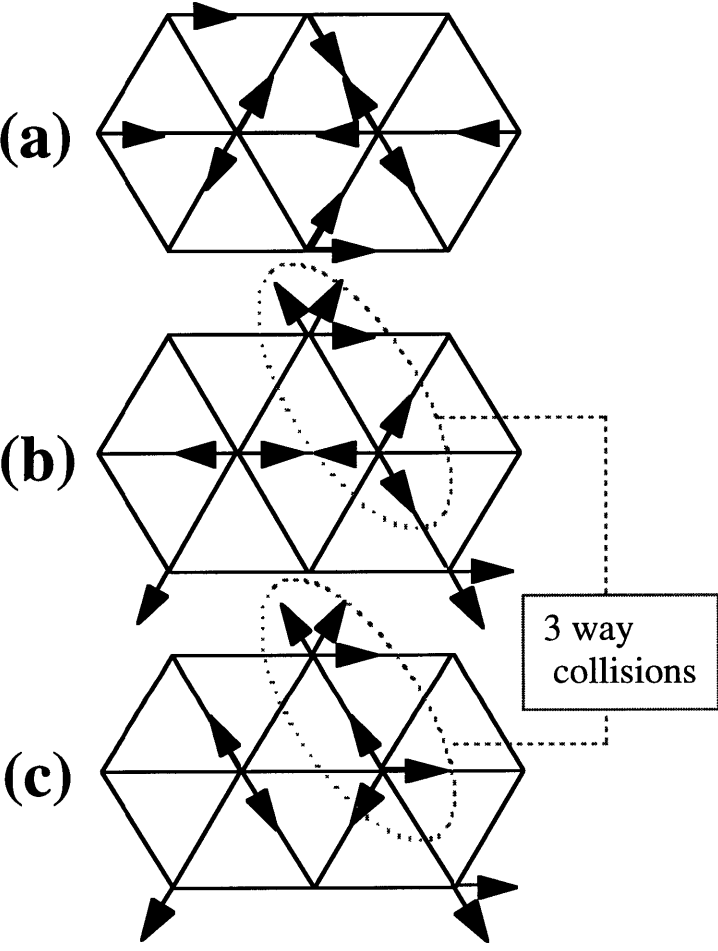


Figure 2-1 In the figure, momentum of each particle is illustrated by an arrow [6]. Propagation is illustrated by (a) and (b). Mass and momentum conserving collision is illustrated by (b) and (c).

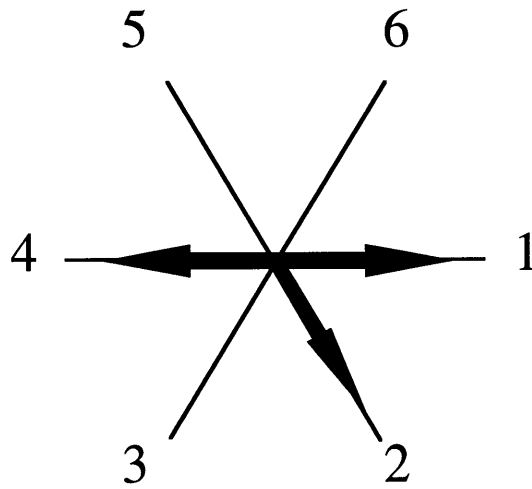


Figure 2-2 Illustration for $\vec{n} = (1,1,0,1,0,0)$.

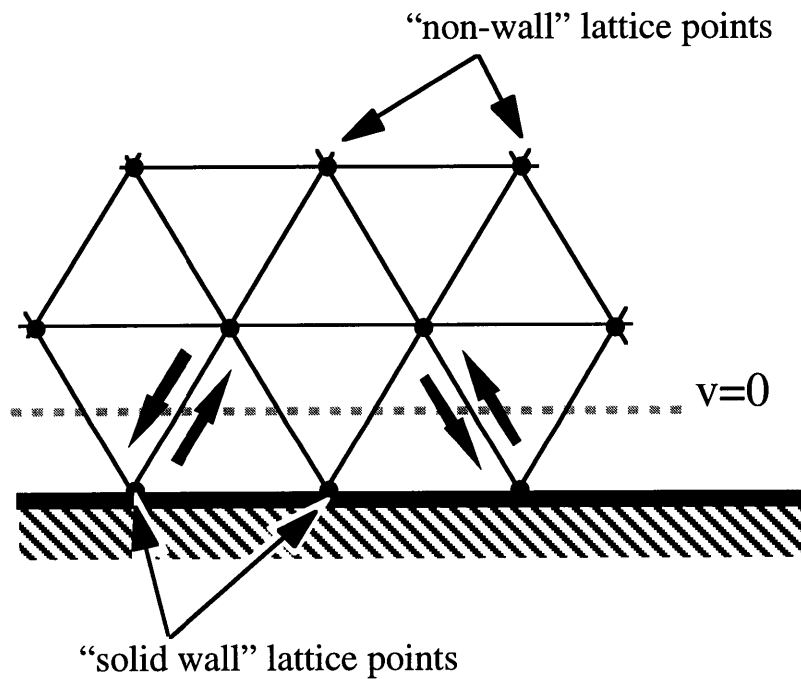


Figure 2-3 No slip boundary condition is created by a simple bounce back rule. On average, velocity at approximately halfway between “wall” lattices and non-wall neighboring lattices becomes zero.

Lattice-gas automata became of practical interest in modeling multi-component fluid dynamics when Rothman and Keller [9] introduced a two-phase immiscible model. In their model, red and blue particles, which represent the two phases, are redistributed after mass and momentum-conserving collisions so that red particles move toward red concentrated directions and blue particles move towards blue concentrated directions as shown in Figure 2-4. Due to inherent fluctuation in the model, spinodal decomposition is exhibited naturally. Interfacial tension can be controlled by modifying the collision rule so that more or less pressure is created normal to the interface as shown in Figure 2-5 [10]. Because phase separation and interfacial tension formulations remain true to physics at each lattice site at each timestep, the macroscopic flows also exhibit correct physics even for complex cases such as flows with moving and changing phase boundaries. Due to this ability, immiscible lattice-gas automata has been applied to simulate many drop breakup and coalescence experiments in binary mixtures [11, 12, 13]. It has also been modified to simulate three-component systems with different interfacial tensions [14], and to simulate the effect of a surfactant [15].

In spite of the above-described advantages and its ability to parallel process computations rather quickly, the lattice-gas automata model also has some serious disadvantages such as the high level of statistical noise in the model for many applications, and the difficulty of extending the multiphase model from two to three dimensions [7].

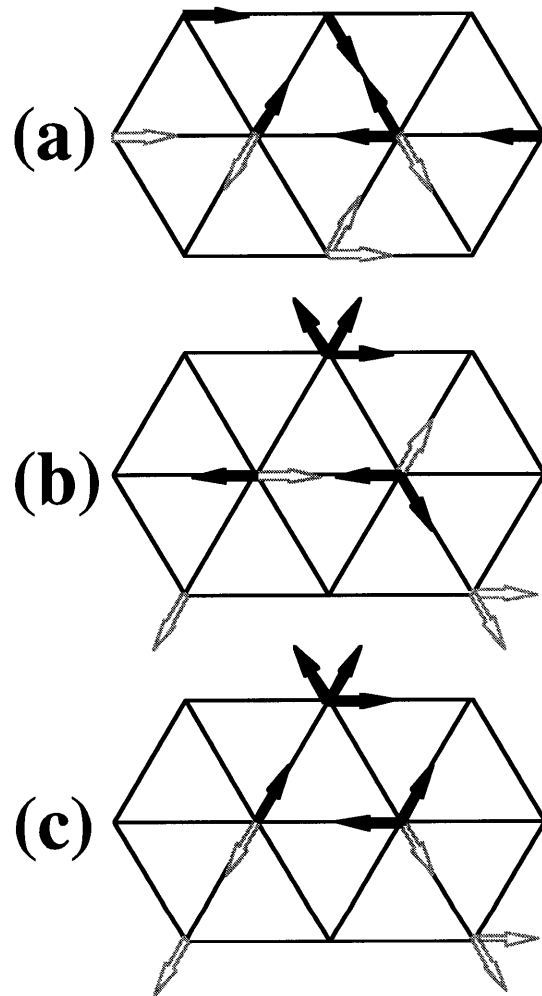


Figure 2-4 In the figure, momentum of red and blue particles are illustrated by black and white arrows [6]. At collisions, red particles go toward red-concentrated direction and blue particles go toward blue-concentrated direction, all while conserving total mass and momentum as illustrated by (b) and (c).

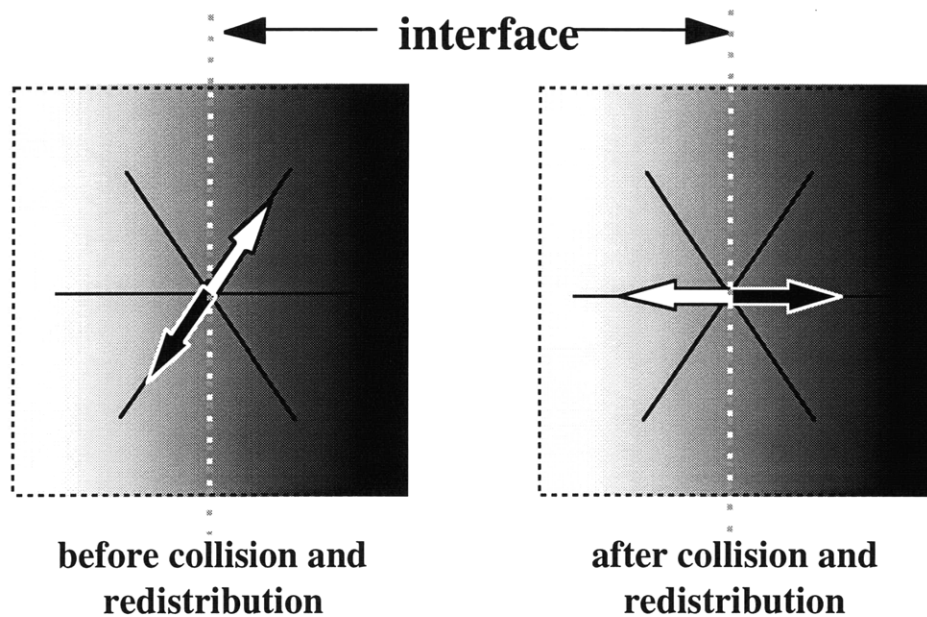


Figure 2-5 Interfacial tension is controlled by controlling the difference between the pressure (density) normal to the interface and the pressure (density) along the interface. The figure below illustrates the collision and redistribution of color when interfacial tension is enhanced.

2.2 Lattice-Boltzmann Method

Aiming to suppress the statistical noise of the lattice-gas model, McNamara and Zanetti [16] introduced the lattice-Boltzmann method in 1988. In contrast to the lattice-gas automata that yields Navier-Stokes hydrodynamics from collision rules and the Boltzmann approximation [6], the lattice-Boltzmann method incorporates hydrodynamics directly since it relaxes the propagated mass probability distribution toward the pseudo-equilibrium distribution that represents the Boltzmann equation. Below is the equation of evolution for the lattice-Boltzmann method:

$$N_i(\bar{x} + \bar{c}_i, t + 1) - N_i(\bar{x}, t) = \sum_j \Lambda_{ij} [N_i(\bar{x}, t), N_i^{(p)}(\bar{x}, t)] \quad (2-5)$$

where $N_i^{(p)}$ is a pseudo-equilibrium operator. The pseudo-equilibrium operator for the case where no rest particle is used in the lattice is given by

$$N_i^{(p)} = f \left[1 + \frac{c_{i\alpha} u_\alpha}{c_s^2} + G_m Q_{i\alpha\beta} u_\alpha u_\beta \right] \quad (2-6)$$

where

$$f = \rho/b \quad (2-7)$$

$$c_s^2 = c^2/D \quad (2-8)$$

$$Q_{i\alpha\beta} = c_{i\alpha} c_{i\beta} - \frac{c^2}{D} \delta_{\alpha\beta} \quad (2-9)$$

ρ is the density and is the sum of mass probabilities in all lattice directions at a lattice point. b is the number of lattice directions and is 6 for the two-dimensional (2D) hexagonal lattice shown in Figure 2-1 and is 24 for three-dimensional face-centered hyper-cubic (FCHC) lattice geometry. f is called the reduced density and is an average mass probability per lattice direction. c_s is the speed of sound propagation within the medium. D represents the number of dimensions and is 2 for a 2D lattice but is 4 for a 3D rendering of a FCHC lattice since the FCHC lattice itself has a fourth dimension. The details of FCHC lattice geometry are discussed by Rothman [6]. $c = |\bar{c}_i|$ is the propagation velocity, defined as lattice length/timestep, and is 1 for a 2D lattice, and $\sqrt{2}$ for the FCHC lattice. G_m is an adjustable parameter.

The lattice-Boltzmann derivative of lattice-gas automata still uses a discrete lattice, discrete timesteps, and a discrete unit velocity. However, unit mass of lattice-gas automata

is replaced with floating point mass probabilities. An immiscible lattice-Boltzmann model soon followed [7] using similar concepts for phase separation and interfacial tension formulations as the lattice-gas automata did. In the immiscible lattice-Boltzmann method, interfacial tension can be explicitly varied and analytically predicted, as opposed to lattice-gas automata which does not have any analytical expression of interfacial tension [17].

Although it has a few disadvantages, primarily slower simulation speed due to its floating point mass probabilities, the lattice-Boltzmann method successfully removes the statistical noise of the lattice-gas automata while preserving significant advantages of the lattice-gas method such as its ability to handle complex boundary conditions and its ability to simulate moving boundaries in binary mixtures. Since the lattice-Boltzmann method does not depend on discrete collision rules for viscosity and interfacial tension formulation and does not require time or spatial averaging, it is superior in manipulating these two fluid dynamical parameters as well. The speed of simulation was improved by the introduction of the BGK lattice-Boltzmann method based on theory by Bhatnagar, Gross and Krook [18], which closely approximates to Navier-Stokes hydrodynamics while using only one relaxation parameter. Another major disadvantage of the lattice-gas automata, the difficulty in extending it to three dimensions, as noted by Rothman, was also overcome using the lattice-Boltzmann method. The FCHC lattice formulation [19], which computes in four dimensions and projects back to three dimensions, is the most commonly used 3D lattice in order to maintain the isotropy of the stress tensor.

Its flexibility in manipulating fluid dynamics parameters and its ability to simulate in three dimensions has led to the lattice-Boltzmann method being verified and applied in many applications by researchers in different fields. Among notable experiments from a polymer processing perspective are; droplet deformation in simple shear [20], pressure

flow between parallel plates using power-law fluids [21], and observation of cavity flow [22].

3. Quantitative Verification of the Lattice-Boltzmann Method

3.1 Simulation Setup

The author has conducted several lattice-Boltzmann simulations in order to quantitatively verify the method's accuracy in exhibiting the fluid dynamic parameters that are important in polymer processing. The lattice-Boltzmann method used is the BGK lattice-Boltzmann method with a single relaxation parameter and no rest particle. The equation of evolution [6] is given by:

$$N_i(\bar{x} + \bar{c}_i, t + 1) = (1 + \delta)N_i(\bar{x}, t) - \delta N_i^{(p)}(\bar{x}, t) \quad (3-1)$$

where $N_i^{(p)}$ is given by the equation (2-6). δ is the single relaxation parameter which is related to the fluid's kinematic viscosity [6] by:

$$\nu = \frac{c^2}{D+2} \left(-\frac{1}{\delta} - \frac{1}{2} \right) \quad (3-2)$$

where ν is the kinematic viscosity. c and D are defined in the previous section. The present author reworked a single-relaxation single-phase 3D FCHC lattice-Boltzmann code written by O. A. van Genabeek into a two-phase 3D simulation program by faithfully implementing and expressing Rothman's [6] scheme for color separation and the formulation of interfacial tension.

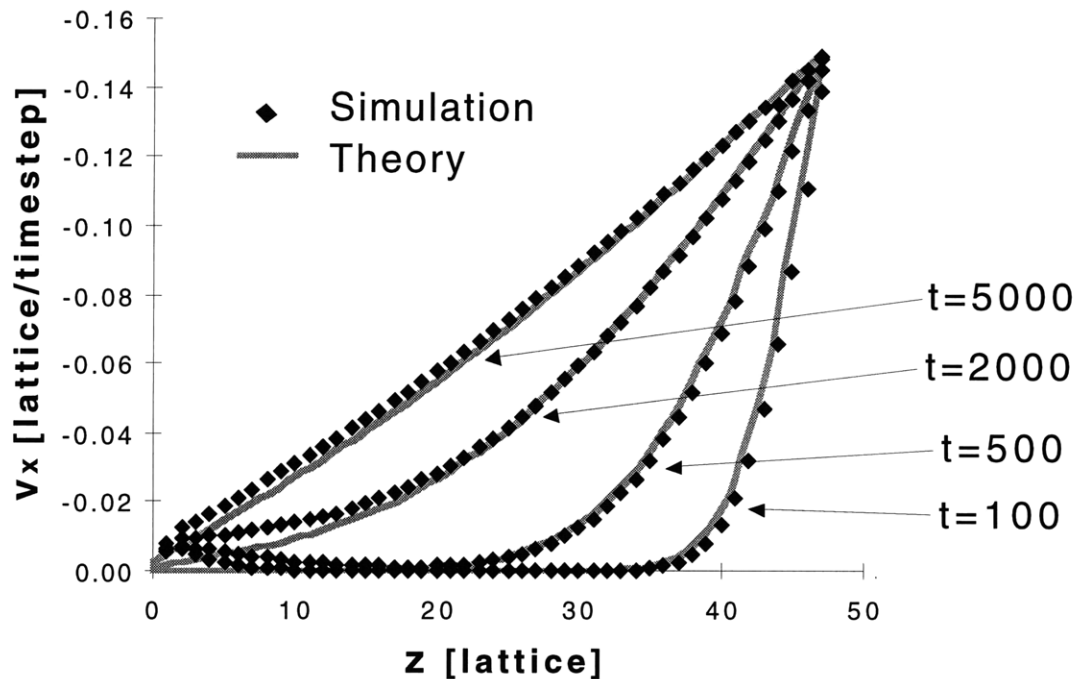


Figure 3-1 Velocity profile of a drag flow between parallel plates with the right plate suddenly set in motion in the x direction. The fluid is Newtonian and was initially at rest.

3.2 Drag Flow Between Parallel Plates with One Plate Suddenly Set in Motion

The startup of drag flow between parallel plates simulation was performed to confirm the velocity evolution with respect to time as well as to confirm the validity of the shear viscosity in the simulation. Some existing simulations can simulate equilibrium states of particular flows correctly, but are erroneous when used come to simulating transient states. When simulating the complex, multiphase, moving boundary flows often seen in polymer processing, this type of shortcoming is intolerable.

Initially, a fluid between parallel plates at $z=0$ and $z=z_0$ is at rest. The velocity $v_x(z)$ measured as the right plate at $z=z_0$ is moved at constant velocity V in the x direction. The analytical solution [23] for $v_x(z, t)$ is given by:

$$v(z, t) = V \left(1 - \frac{z}{z_0} \right) - \frac{2V}{\pi} \sum_{i=1}^{\infty} \frac{1}{i} \exp \left(-i^2 \pi^2 \frac{vt}{z_0^2} \right) \sin \left(i\pi \frac{z}{z_0} \right) \quad (3-3)$$

In the lattice-Boltzmann simulation, bounce-back of mass distribution is biased so that $v_x(z=z_0)$ becomes V , making the wall appear to move. The same simulation using the lattice-Boltzmann method with a 2D hexagonal lattice was previously conducted by Szilágyi, Susan-Resiga and Sofonea [24]. Using the single phase 3D FHC lattice-Boltzmann method, the present author has also proven the agreement of the simulation results with the theory as shown in Figure 3-1. The simulation was conducted using $100 \times 2 \times 50$ lattices with periodic boundary in all directions and $\eta=0.1$ and $\rho=1$.

3.3 Pressure Flow Between Parallel Plates of a Newtonian Fluid

Many polymer processing flows are pressure driven flows. The simplest of pressure flows is the flow between parallel plates. Left and right plates at $z=0$ and $z=z_0$ are rigid no-slip walls, and the pressure is exerted at one end ($x=0$) and the flow comes out at another ($x=x_0$). The pressure difference ΔP over distance x_0 is what forces the flow to move in the x direction. The velocity of the fluid at the walls, $v_x(z=0)$ and $v_x(z=z_0)$, is zero and has its maximum $v_{x,\max}$ at $z=z_0/2$. In the case of a Newtonian fluid, the analytical solution [25] for $v_x(z)$ is given by:

$$v_x = \left(\frac{z_0^2 \Delta P}{8\eta x_0} \right) \cdot \frac{4z}{z_0} \left(1 - \frac{z}{z_0} \right) \quad (3-4)$$

and

$$v_{x,\max} = \frac{z_0^2 \Delta P}{8\eta x_0} \quad (3-5)$$

In the present lattice-Boltzmann simulations, the total bounce-back rule is applied at both walls. Pressure is created by adding an extra mass distribution at one end ($x=0$) and removing the same amount at the other end ($x=x_0$). Pressure in the particular single-relaxation lattice-Boltzmann model [6] used is given by:

$$p(\rho) = c_s^2 \rho \quad (3-6)$$

and is $\rho/2$ for the 3D FCHC lattice-Boltzmann model with no rest particles. The simulations were run until they reached the equilibrium and $v_x(z)$ was measured at $x=z_0/2$. At equilibrium state, $\Delta P/z_0$ can be obtained by measuring density at any two points of different x .

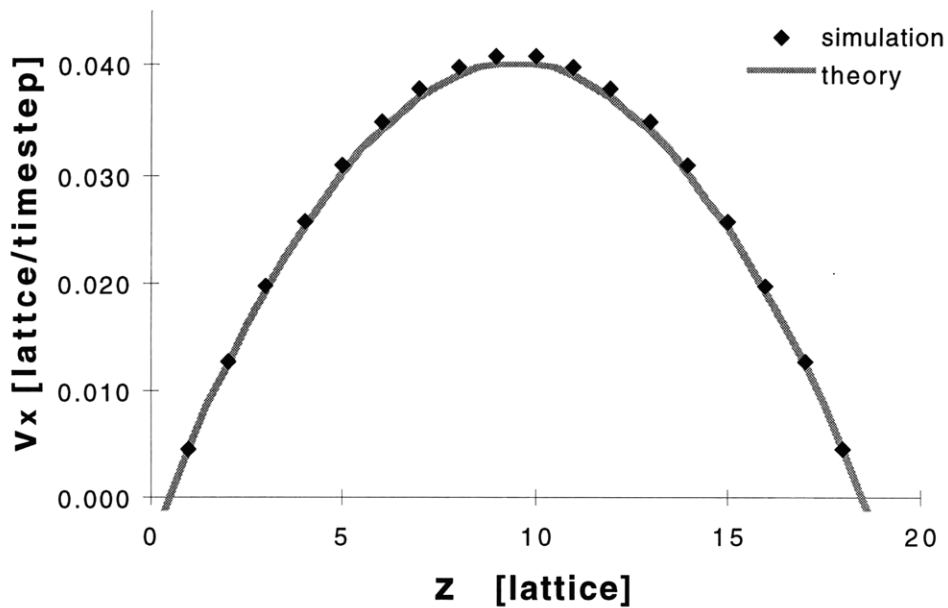


Figure 3-2 Velocity profile of pressure flow between parallel plates. The fluid is Newtonian.

This simulation has been conducted and validated previously [26]. The author has also verified the simulation's shear viscosity and pressure by varying viscosity, lattice dimensions, and pressure using a single-phase viscous fluid. As shown in Figure 3-2, the simulation is in a good agreement with the theory when the kinematic viscosity ν is approximately 0.1 or less. A higher than expected $v_{x,max}$ is observed when ν is set at higher values. When ν is assigned as 0.5 or higher, the velocity profile is no longer a smooth parabola. This observation can be explained as follows: The relaxation parameter δ is related to ν by equation (3-2). The mean free path of the mass distribution is approximately $1/|\delta|$. Therefore, as ν becomes larger, so does the mean free path. When the mean free path becomes larger with respect to the unit lattice length, the correct relaxation to a pseudo-equilibrium distribution cannot be achieved because gradual changes in the distribution are prohibited. This was observed when ν reached 0.5 ($-\delta = 0.5$). Relative to the mean free path, the higher than expected $v_{x,max}$ comes from the assumption that the zero velocity point or virtual wall lies halfway between the solid wall lattice point, and the nearest neighboring non-wall lattice point as illustrated in Figure 3-3. The detailed analysis of population density and velocity by Ginzbourg and Adler [27] suggests that the assumption of the virtual wall at the halfway location becomes inaccurate when the mean free path becomes longer. Their analysis of Poiseuille flow using the FHC lattice-Boltzmann method shows that the zero velocity location shifts toward the solid wall lattice point as mean free path becomes longer. This is due to the density difference between the solid wall lattice point and the neighboring non-wall lattice point created by the longer mean free path. When the correct zero velocity boundary is applied, the simulation agrees with the analytical solution as shown in Figure 3-3.

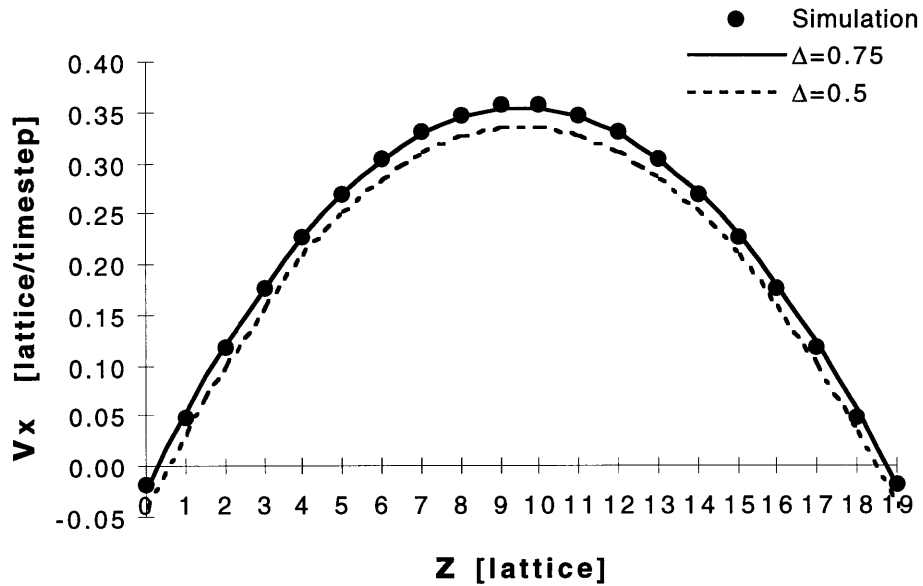


Figure 3-3 Example of the deviation of $v_{x,max}$ at larger $-1/\delta$ when the ‘halfway’ boundary condition is applied. The simulation agreed with the analytic solution at the correct zero velocity location. Δ is a distance between the first non-wall lattice point and the virtual wall boundary created by the bounce-back rule.

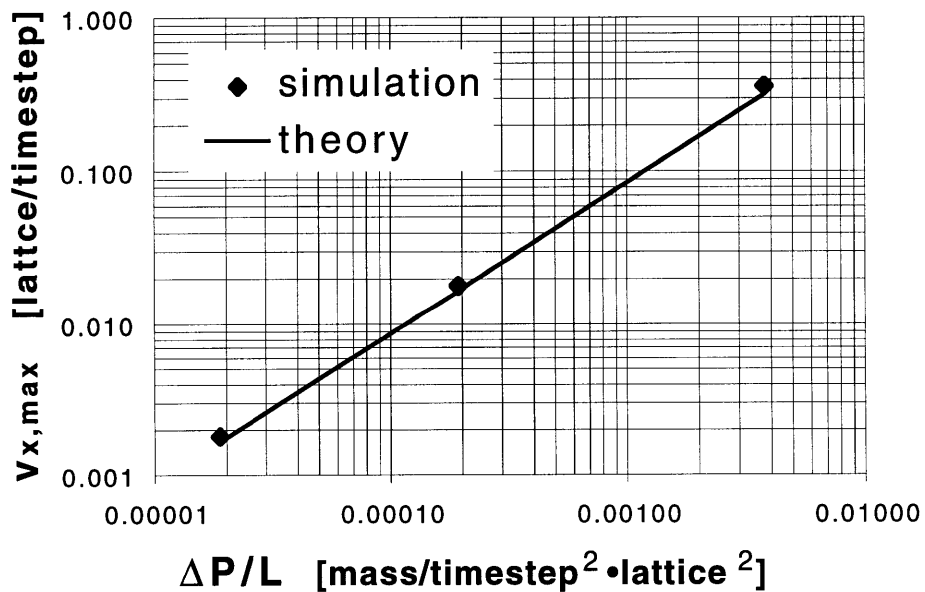


Figure 3-4 The linearity of the relationship between the pressure gradient and $v_{x,max}$ for Newtonian pressure flow as expressed in equation (3-4) is confirmed.

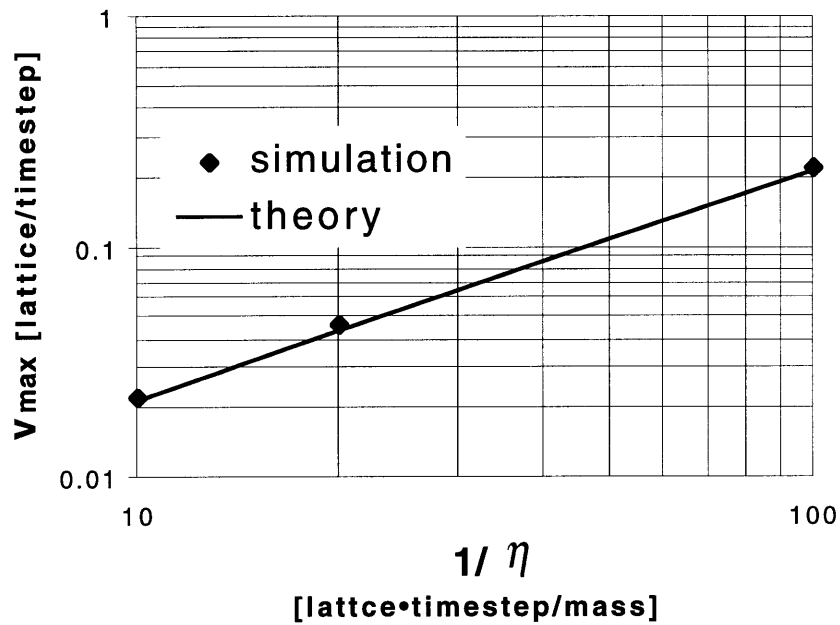


Figure 3-5 The linearity of the relationship between $1/\eta$ and $v_{x,max}$ for Newtonian pressure flow as expressed in equation (3-4) is confirmed.

Linear relationships between $v_{x,max}$ and $\Delta P/x_0$, and between $v_{x,max}$ and $1/\eta$ are also confirmed by the simulations as shown in Figures 3-4 and 3-5.

3.4 Pressure Flow Between Parallel Plates of a Power-Law Fluid

Unlike fluids such as water and air, whose viscosities are independent of shear rate, the viscosity of most polymers is affected by shear rate. This dependence is often approximated by the power-law rule [25] as follows:

$$\eta(\dot{\gamma}) = m\dot{\gamma}^{n-1} \quad (3-7)$$

where m and n are the consistency and power law index, respectively. For many materials, such as polystyrene, there can be both a “Newtonian plateau” at smaller shear rates and a “power law” region at higher shear rates [28].

In the 3D lattice-Boltzmann simulation, shear rate is calculated locally at each lattice point by

$$\dot{\gamma} = \sqrt{\frac{1}{2} \dot{\gamma} : \dot{\gamma}} \quad (3-8)$$

or, in expanded form:

$$\dot{\gamma} = \left[2 \left(\frac{\partial v_x}{\partial x} \right)^2 + 2 \left(\frac{\partial v_y}{\partial y} \right)^2 + 2 \left(\frac{\partial v_z}{\partial z} \right)^2 + \left(\frac{\partial v_y}{\partial x} + \frac{\partial v_x}{\partial y} \right)^2 + \left(\frac{\partial v_y}{\partial z} + \frac{\partial v_z}{\partial y} \right)^2 + \left(\frac{\partial v_z}{\partial x} + \frac{\partial v_x}{\partial z} \right)^2 \right]^{1/2} \quad (3-9)$$

where $\partial v_x / \partial x = v_x(x+1, x-1) / 2\sqrt{2}$ and so on. The relaxation parameter is modified according to equation (3-7) using the local shear rate given above.

Simulation of pressure flow through parallel plates of a power-law fluid was previously conducted by Rothman and Aharonov [21] and agreed with the theoretical velocity profile [25] given by:

$$v_x = \frac{z_0}{2(s+1)} \left(\frac{z_0 \Delta P}{2mx_0} \right)^s \left[1 - \left(\frac{2z}{z_0} - 1 \right)^{s+1} \right] \quad (3-10)$$

where $s=1/n$. The author also simulated pressure flow of a single phase power-law fluid with power law indices of 1.5 and 0.6, and observed a very good agreement with the theory as shown in Figures 3-6 and 3-7. When conducting simulations, the same care with ν must be taken in order not to make the mean free particle path too long with respect to the lattice.

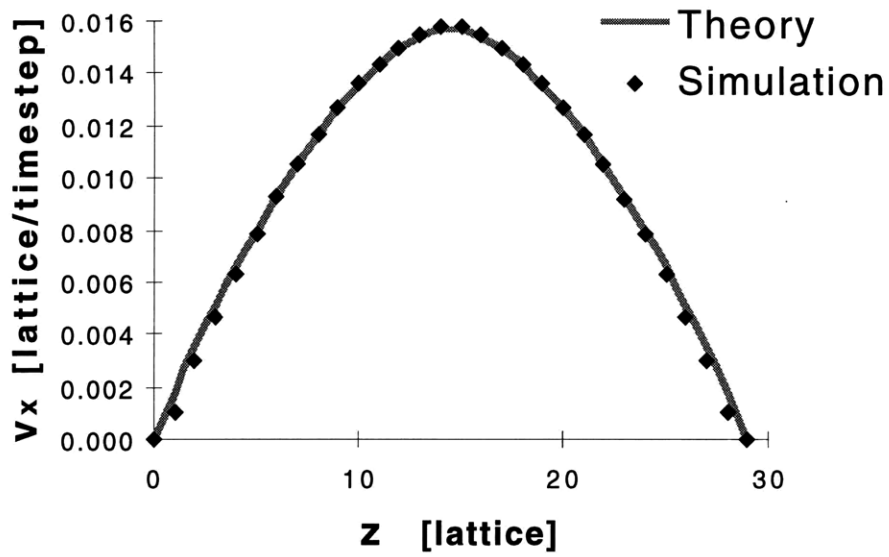


Figure 3-6 The velocity profile of pressure flow between parallel plates for a non-Newtonian fluid. The fluid is a power law fluid with a power law index of 1.5.

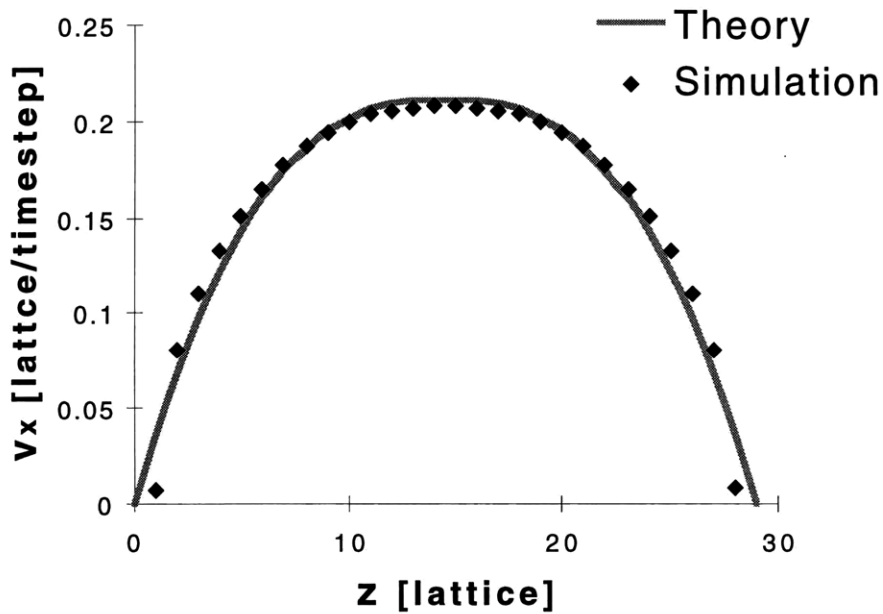


Figure 3-7 The velocity profile of pressure flow between parallel plates for a non-Newtonian fluid. The fluid is a power law fluid with a power law index of 0.6.

3.5 Steady State Sphere and Cylinder (Laplace's Law)

In a multiphase fluid, the interfacial tension is of great importance in breakup and coalescence events. At steady state, the relationship between the curvature of an interface, the interfacial tension, and pressure is given by Laplace's Law:

$$\Delta P = \sigma \left(\frac{1}{R_1} + \frac{1}{R_2} \right) \quad (3-11)$$

where σ is interfacial tension, ΔP is the pressure difference between the phases, and $1/R_1$ and $1/R_2$ are the principal radii of curvature. For cases of a circle in two dimensions or a cylinder in three dimensions, the above equation becomes

$$\Delta P = \frac{\sigma}{R} \quad (3-12)$$

where R is the radius of circle or cylinder. For the case of a sphere in three dimensions, it becomes

$$\Delta P = \frac{2\sigma}{R} \quad (3-13)$$

where R is the radius of sphere.

Interfacial tension in the lattice-Boltzmann method in three dimensions [6] is given by:

$$\sigma = -\frac{4608Af}{\delta} \quad (3-14)$$

where A is an adjustable parameter used to create pressure normal to interface, f is a reduced density per lattice direction, and δ is the relaxation parameter. The interfacial tension used in the lattice-Boltzmann method has been confirmed by many researchers using Laplace's Law and a spherical droplet in a quiescent matrix [17, 29]. Comparisons

of the expected interfacial tension σ calculated from equation (3-11) and simulation output of σ calculated from equation (3-14) at various A , f , δ are summarized in Figures 3-8, 3-9, and 3-10 for the sphere (3-D Laplace's Law). Deviation from the analytical value is observed when the value of $-1/\delta$ becomes larger than unity. This is easily explained. As discussed previously, $-1/\delta$ is approximately the mean free path of the mass distribution. At the interface, the path of a mass distribution can be changed even if the relaxation parameter is set 0 ($-1/\delta = \infty$) due to the color separation step at the collision. In other words, at the interface, the actual mean free path (or $-1/\delta$) can be shorter than the input value of δ indicates. Figure 3-10 shows that the larger the value of $-1/\delta$, the more the simulation results deviate from the analytical solution. The deviation starts at $-1/\delta \approx 0.9$, where the mean free path is becoming large with respect to the lattice. The fact that the model's interfacial tension accurately follows its analytical expression has been confirmed when $-1/\delta < 0.8$ ($v < 0.1$).

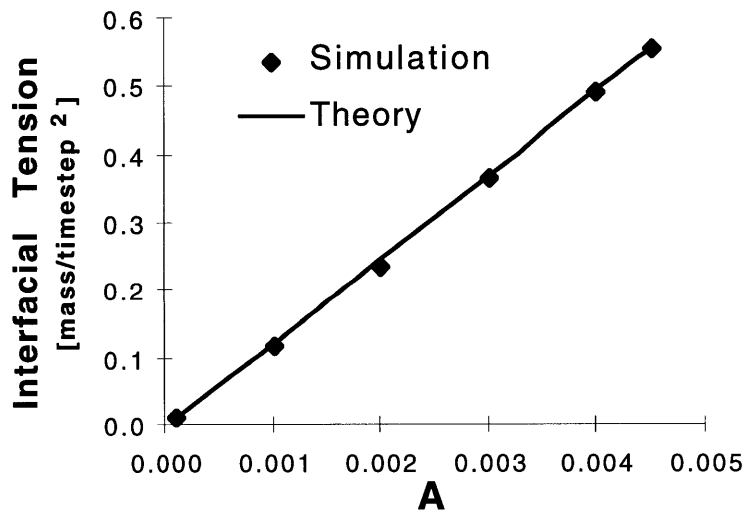


Figure 3-8 A is a variable in the lattice-Boltzmann method that creates pressure normal to the interface. The figure shows the linear relation between interfacial tension and A as expected from equation (3-14).

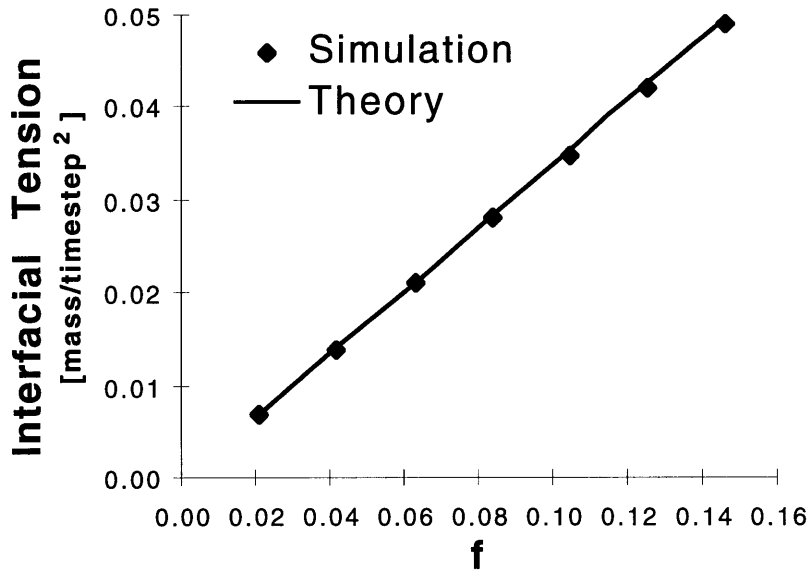


Figure 3-9 f is the reduced density, or an average mass probability per lattice direction at a lattice point. The figure shows the linear relation between the interfacial tension and f as expected from equation (3-14).

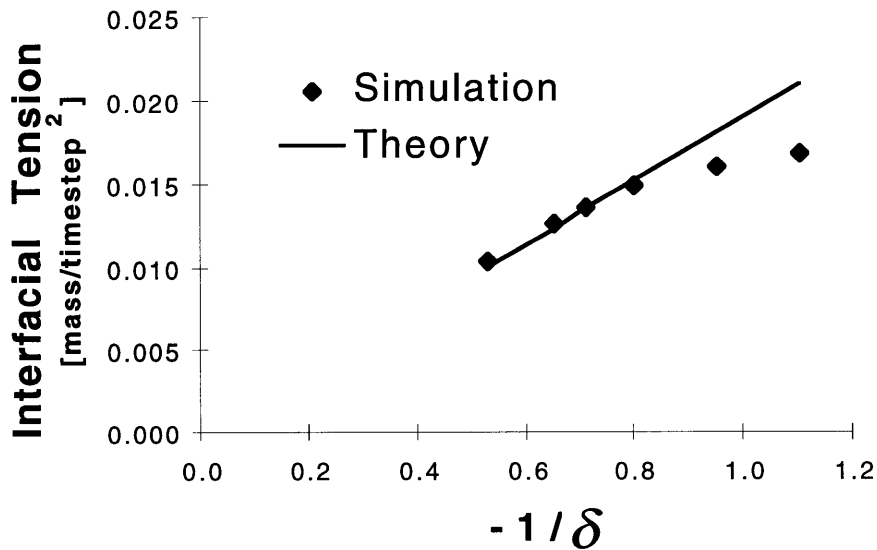


Figure 3-10 δ is the relaxation parameter in the lattice-Boltzmann method. $-1/\delta$ is expected to show the linear proportionality to the strength of interfacial tension when everything else is held constant. The deviation at larger $-1/\delta$ shows the lower limit of $|\rho|$ allowed for a given lattice.

3.6 Deformation of a Droplet in Simple Shear Flow

A droplet deforms before it breaks. Deformation of a droplet involves multiple hydrodynamic parameters such as interfacial tension, shear rate, viscosity, and so on. Therefore, it is important for any simulation technique to exhibit the correct morphology of the deformation. The small deformation of a droplet in shear flow, in the case in which both the droplet phase and the matrix phase are Newtonian fluids, was first studied by Taylor [30]. The deformation of such a droplet is given by the equation:

$$D_d = \frac{\eta \dot{\gamma} R}{\sigma} \left(\frac{19\eta'/\eta + 16}{16\eta'/\eta + 16} \right) \quad (3-15)$$

where η is the viscosity of the matrix phase, $\dot{\gamma}$ is the shear rate, R is the initial droplet radius, σ is the interfacial tension and η'/η is the ratio of the viscosities of the dispersed phase and the matrix phase. The degree of deformation is described by the parameter D_d which is given by

$$D_d = \frac{b - a}{b + a} \quad (3-16)$$

where b is the length and a is the breadth of the ellipsoid as shown in Figure 3-11. Experimentally, deformation of the droplet follows Taylor's small deformation theory up to around $D_d=0.2$ when $\eta'/\eta=1$ [31].

Two-dimensional lattice-Boltzmann simulation of small droplet deformation has been carried out by Halliday and Care at various shear rates and interfacial tensions [20]. Using the 3D lattice-Boltzmann method with no rest particles, the author has measured the deformation of a droplet with respect to capillary number at varying shear rates, interfacial tensions, and drop radii. The capillary number, a ratio of the viscous droplet breakup forces to interfacial stabilization forces, is defined as:

$$Ca = \frac{\eta \dot{\gamma} R_0}{\sigma} \quad (3-17)$$

A typical deformation of a droplet in 3-D is shown in Figure 3-12. The present author has successfully observed the linear relationship with a slope of $(19\eta'/\eta + 16)/(16\eta'/\eta + 16)$ in the simulation as shown in Figure 3-13.

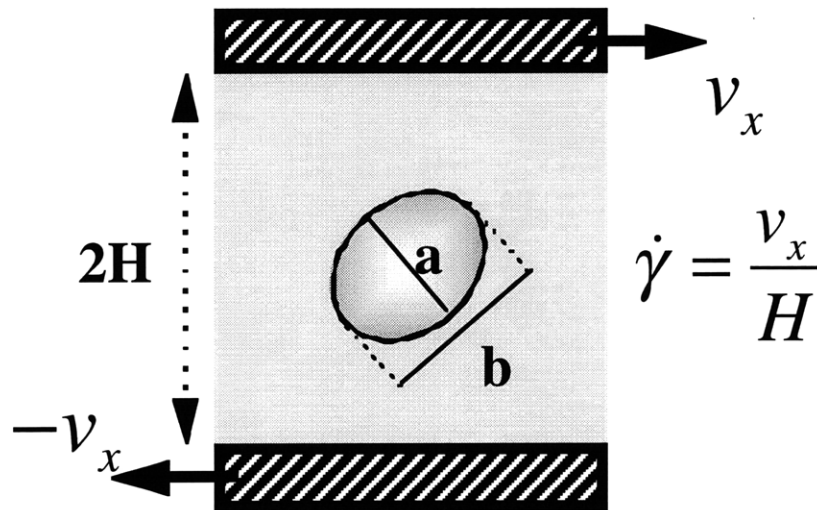


Figure 3-11 Illustration of a 2D projection of a 3D droplet deformation in a simple shear flow. The ellipsoid has the same breadth, a , in the third dimension.

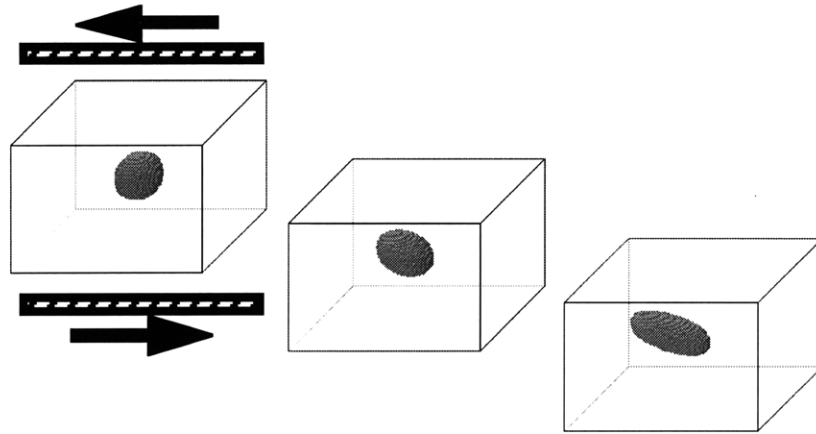


Figure 3-12 3D visualization of the deformation of a droplet simulated by 3D lattice-Boltzmann method.

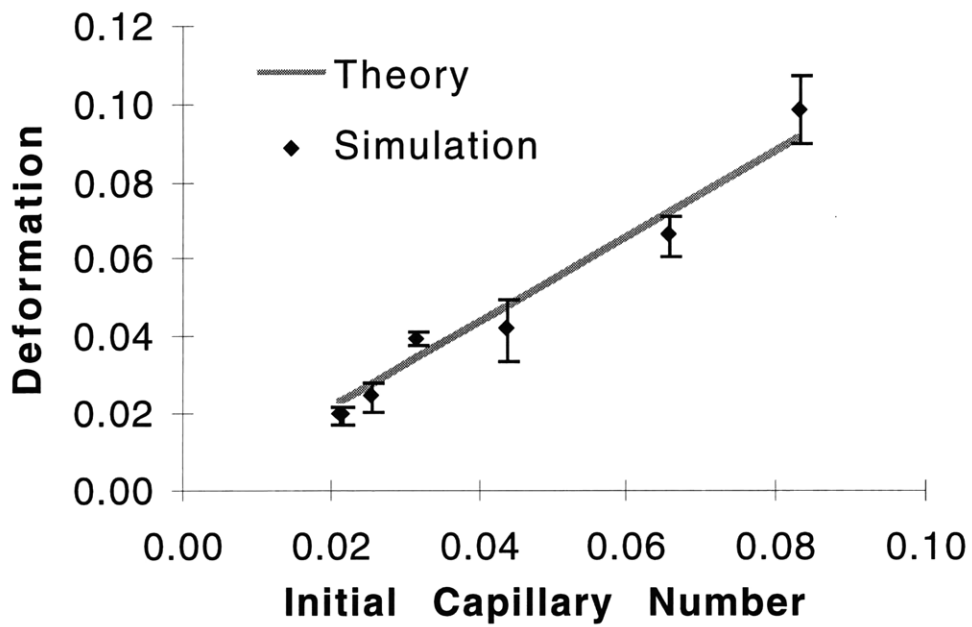


Figure 3-13 Deformation of a droplet with respect to initial capillary number. For small amounts of deformation, a linear relationship is predicted by Taylor's small deformation theory.

4. Capillary Wave Instability

4-1 Introduction

Experimentally, a highly elongated droplet (which is almost like a long cylinder) has been observed to breakup into many small, evenly sized droplets when the stress is relaxed [32]. Although the quiescent state of a fluid is not of direct interest in simulating polymer processing flows, Kang, et. al. have pointed out that this type of situation could occur in cavity flow [33].

The breakup of a cylindrical thread was first analyzed by Rayleigh [34] for a fluid cylinder in air. Tomotika [35] extended the theoretical analysis to the breakup of a viscous fluid thread in a viscous matrix phase.

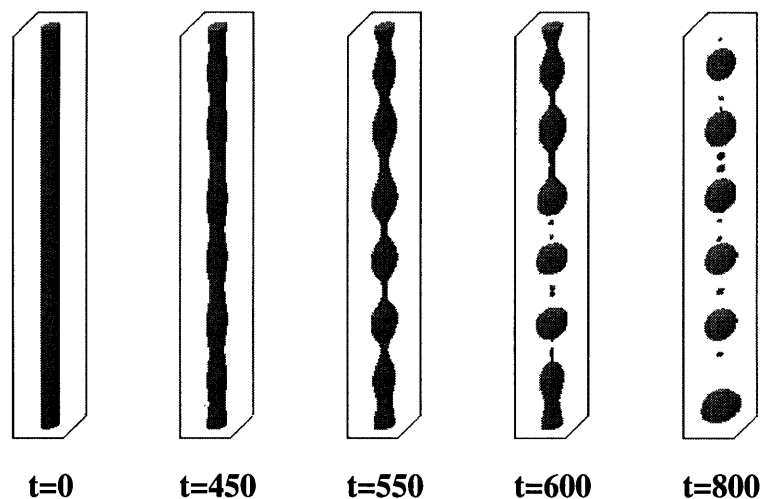


Figure 4-1 A typical rendering of capillary wave instability simulated by 3D lattice-Boltzmann simulation. A certain wavelength grows from random noise added to the simulation.

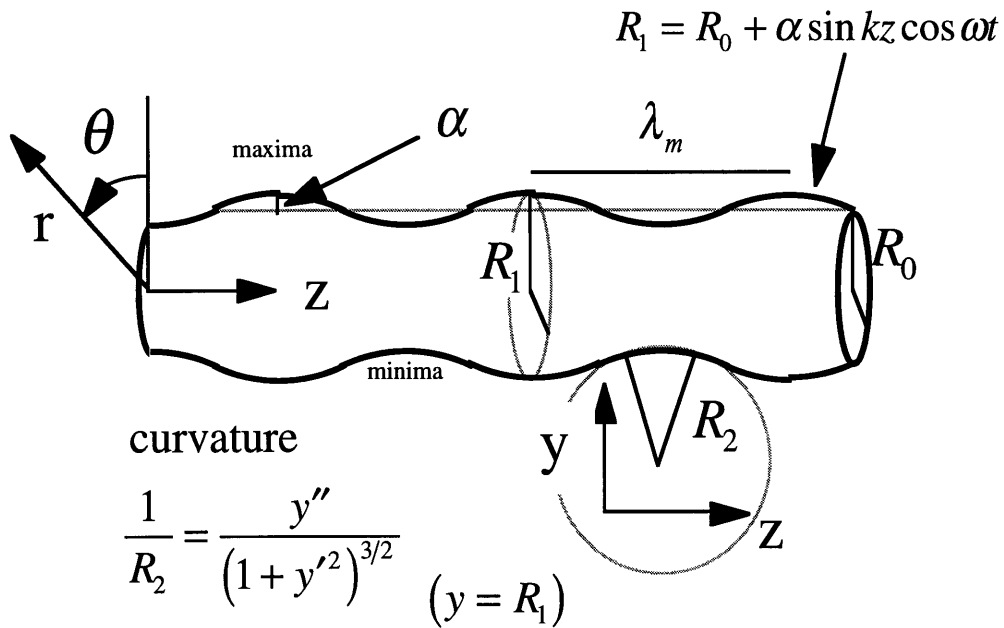


Figure 4-2 Illustration and nomenclature of the capillary wave disturbance.

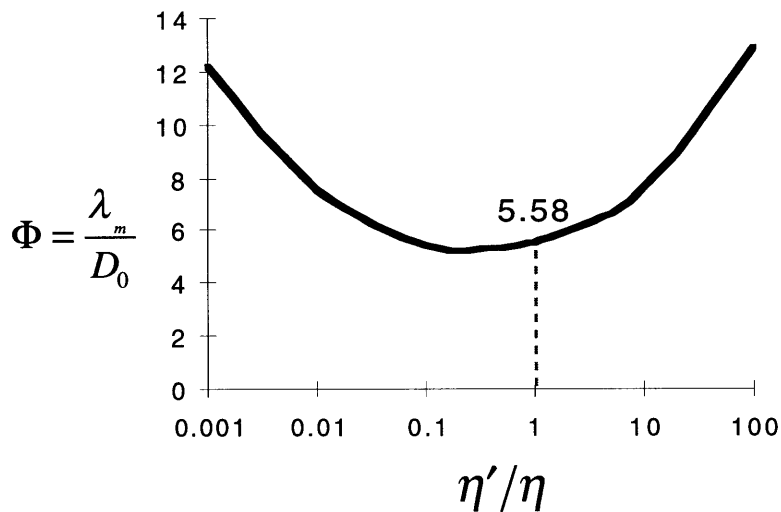


Figure 4-3 The fastest growing disturbance wavelength as a function of viscosity ratio, based on Tomotika's [35] data.

Brownian motion introduces infinitesimal perturbations on the surface of the cylinder. These perturbations are considered as a collection of disturbances of many wave lengths. Stability analysis is applied to distinguish which disturbing wavelengths will grow and which will decay away. It is found that any wavelength longer than the circumference of the cylinder is unstable and grows. Among wavelengths longer than the circumference, a particular wavelength determined by the initial diameter of a cylinder and the viscosity ratio, has the largest exponential growth rate. It is primarily this wavelength that breaks the cylinder into small evenly sized droplets as shown in Figure 4-1 and 4-2. The fastest growing wavelength λ_m as a function of η'/η is shown in Figure 4-3. For example, λ_m is 5.58 times the diameter of the cylinder at $\eta'/\eta=1$. The disturbance amplitude α grows exponentially as

$$\alpha = \alpha_0 e^{qt} \quad (4-1)$$

where α_0 is the initial disturbance amplitude and q is the rate of growth [36] given by:

$$q = \frac{\sigma\Omega(\lambda, \eta'/\eta)}{2\eta R_0} \quad (4-2)$$

Ω is a tabulated function of wavelength and the viscosity ratio given in Tomotika's [35] paper. Figure 4-4 shows the relationship between the growth rate and its wavelength at $\eta'/\eta = 1$. One can calculate the interfacial tension between any given two phases of fluid by measuring the growth rate, q , using the above equation if the viscosity of both phases is known. This method is often used for measuring interfacial tension between two polymers [36]. Compared with other interfacial tension determination methods, such as the pendant drop method [37], the spinning drop method [38], and the sessile drop method [39], all of which require measurements in the equilibrium state, measurements in this breaking-thread

method are much faster since they are done under transient conditions. For interfacial tension measurements of slowly evolving viscous fluids such as polymers, the breaking-thread method allows more time efficient measurements.

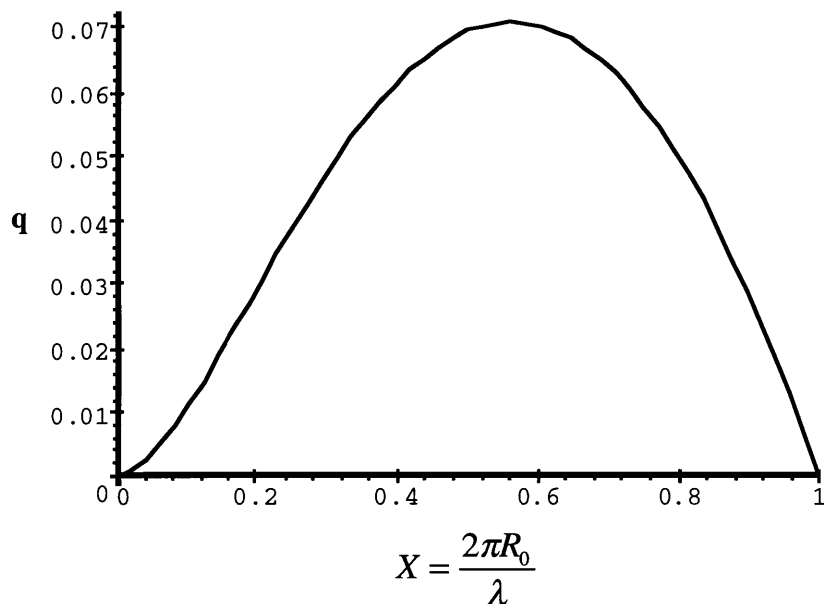


Figure 4-4 Growth rate (q) as a function of X at a viscosity ratio of one. X is defined as shown above.

4-2 Perturbations in the Lattice-Boltzmann Method

Since simulation of an infinitely long cylinder is not possible, the author used a 35x35x300 lattice or similar dimensions with periodic boundaries in all directions, and an initial cylinder radius of around 6 lattice units. For convenience, the interfacial tension was chosen large enough so that breakup occurred within 500 - 2000 timesteps. In real life, random disturbances are caused by Brownian motion. Unlike the lattice-gas automata,

which has intrinsic noise, the lattice-Boltzmann method itself does not have any built-in noise. Therefore, no breakup would occur if a cylinder is left unperturbed in the regular lattice-Boltzmann simulation environment. Hence, random disturbances must be externally enforced in the simulation in order to imitate the effect of random perturbations. Several methods for formulating random disturbances were investigated.

The initial method studied involved perturbing the momentum of each lattice direction at each interface lattice point randomly. While yielding a nice thread breakup as shown in Figure 4-1, and conserving mass and momentum when sufficient time or spatial averaging is used, this method conserves neither mass nor momentum at each lattice point at each timestep. The second method considered fluctuates the local density at each lattice site. This also resulted in thread breakup, but does not conserve mass locally.

The direction of the interface in the lattice-Boltzmann method is defined by its normal vector \vec{f} . This vector, also known as the local color gradient, points to the direction where the probability of finding red particles is the highest [6], and is given by:

$$\vec{f}(x,t) = \sum_i \vec{c}_i \sum_j [R_j(\vec{x} + \vec{c}_i, t) - B_j(\vec{x} + \vec{c}_i, t)] \quad (4-3)$$

where $R_i(\vec{x}, t)$ and $B_i(\vec{x}, t)$ are mass probability at the lattice site \vec{x} at time t and in i th direction. The third method investigated was to vary the direction of this local color gradient. While this method conserves mass and momentum locally at each timestep, it essentially weakens the effect of interfacial tension and does not have any physical significance. The above three methods were attempted, focusing on thread breakup by creating fluctuations in its radius indirectly through Laplace's relation, but had serious deficiencies.

The method chosen for creating disturbances is a perturbation of momentum at each lattice point while conserving mass and momentum. This was done by perturbing the same amount of mass in pairs of opposite-facing lattice directions, and by making no net change of mass and momentum at each lattice site at each timestep as described in Figure 4-5. Since mass and momentum are conserved locally, the physics of incompressible fluids still applies. In the theory of capillary wave instability, it is only the thread radius that is being fluctuated. However, in real life, the radius is fluctuated since Brownian motion creates local fluctuations of density, which in turn creates a curvature on the interface and thus radius fluctuations. From this stand point, this method of fluctuation formulation is loyal to real life Brownian motion disturbances since the velocity (momentum) directions are the ones that change every timestep.

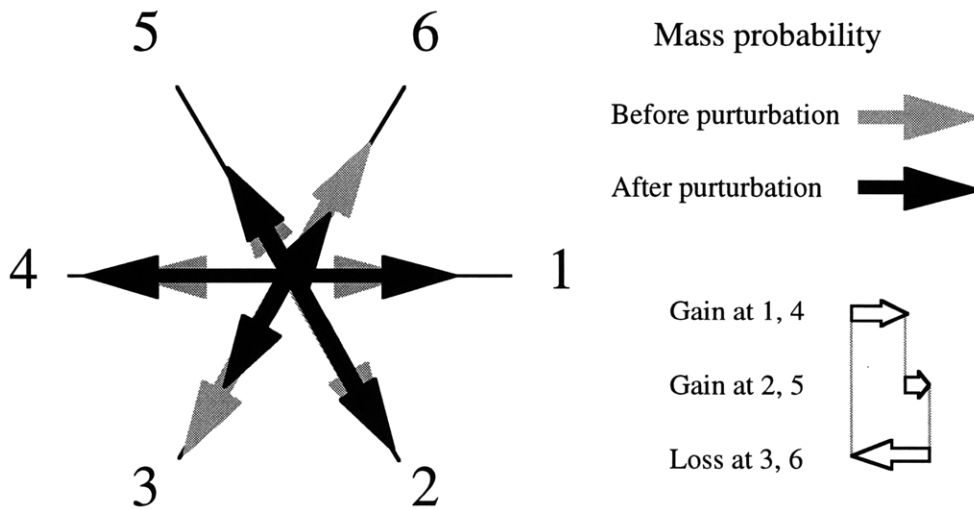


Figure 4-5 Illustration of the random perturbation that conserves mass and momentum in 2D. Lengths of the arrows represent the sizes of mass moving in each direction. Random sizes of mass are added or subtracted to the pair of the opposite facing directions. The random perturbations are added so that there is no net change of the mass at each lattice site, at every timestep.

	Average λ_m [lattice]	Growth Rate, q
theory	62.5	0.0098
1st method	50	0.0050
theory	62.5	0.0150
2nd method	56	0.0066
theory	62.5	0.0057
3rd method	50	0.0022
theory	60	0.0077
4th method	43	0.0046

Table 4-1 Selected simulation results using four different perturbation methods are compared with respective theoretical results. Theoretical growth rates are calculated using the theoretical values of λ_m s. Results by all perturbation methods resulted in shorter than expected wavelengths and smaller than expected growth rate. Shown results are not for use in comparing accuracy of the perturbation methods.

In simulations of capillary wave instability using any of the above four disturbance techniques, breakup of the cylinder was observed but at slower growth rate and with a shorter than predicted wavelength as shown in Table 4-1. In searching for the causes of these deviations from the theory, many simulation modifications including changes in the lattice size, boundary conditions at top and bottom ($z=0$ and $z=z_0$), diameter of the cylinder, viscosity ratio of cylinder/matrix, and interfacial tensions were made. However, no obvious improvement was observed from any of the above modifications.

Since the growth rate is a sensitive function of λ , as shown in Figure 4-4 and equation (4-2), attention was first focused on obtaining the correct λ from the simulation.

In an attempt to observe a thread breakup with λ_m , the author chose to force a standing wave fluctuation rather than random disturbances.

4-3 Forced Perturbation

In real life, the fastest growing wavelength results from a collection of random noise. Since the noise fluctuates over time, such a wave cannot be a sum of time-independent spatially periodic transverse waves. Rather, it is the sum of transverse waves that change over time. At the same time, the fastest growing wave that makes the thread break has fixed nodes where no growth occurs, as observed on the thread. A standing wave is the only transverse wave that has fixed nodes. Based on these two observations, small random fluctuations are considered as the sum of fluctuating standing waves of various wavelengths and periods. A standing wave is created when two propagating transverse waves $r_1 = (\alpha/2)\sin(kz - \omega t)$ and $r_2 = (\alpha/2)\sin(kz + \omega t)$ are superimposed [40], and is given by:

$$R(z,t) = \alpha \sin kz \cos \omega t \quad (4-4)$$

where $k = 2\pi/\lambda$ and $\omega = kv$. v is the propagation speed of a transverse wave.

Since the only mode of wave propagation in a single phase fluid is longitudinal, the propagation speed of a transverse wave at the interface of two fluids can be obtained indirectly from the wave propagation velocities of longitudinal waves as follow. Because a longitudinal wave travels in an elastic media by the compression and decompression of the local media, it can be considered as a propagation of pressure with its amplitude P_M . When a longitudinal wave travels in one medium at velocity v , a local pressure difference ΔP also travels at velocity v as shown in Figure 4-6. When two longitudinal waves in

phase or at different wavelengths travel in two media at the same velocity, the local pressure difference ΔP also travels at velocity v . When the two longitudinal waves travel in two media at different velocities v_1 and v_2 , these waves can be expressed in terms of pressure, and are given by $P_1 = P'_1 + P_m \sin[2\pi(z - v_1 t)/\lambda]$ and $P_2 = P'_2 + P_m \sin[2\pi(z - v_2 t)/\lambda]$. The expression for the pressure difference $\Delta P = P_2 - P_1$ is simplified as

$$\Delta P(z, t) = 2P_m \cos \frac{2\pi}{\lambda} \left[z - \frac{(v_1 + v_2)}{2} t \right] \sin \frac{2\pi}{\lambda} \frac{(v_1 - v_2)}{2} t + (P'_2 - P'_1) \quad (4-5)$$

where $(v_1 + v_2)/2$ is ΔP 's propagation speed. The Laplace relation given by equation (3-11) shows that $\Delta P(z, t)$ creates a transverse wave $\Delta R(z, t)$ whose propagating velocity is the same as that of $\Delta P(z, t)$. In the lattice-Boltzmann simulation, the propagation of a longitudinal wave, which is the speed of sound, is given by equation (2-8). It is $1/\sqrt{2}$ lattice unit per timestep for the FCHC model. Therefore, the propagation velocity of any transverse wave in a 3D lattice-Boltzmann simulation is also $1/\sqrt{2}$ as described in the above case.

Knowing v and λ , a standing wave $\Delta R(z, t)$ is defined. In the lattice-Boltzmann method, however, it is very difficult, if not impossible, to directly create any ΔR while locally conserving mass and momentum. Therefore, $\Delta R(z, t)$ has to be created indirectly from Laplace's relation. Since creating $\Delta P(z, t)$ while conserving mass and momentum is also a very difficult task, the author chose to fluctuate the interfacial tension. Provided that ΔP is constant, $\Delta \sigma(z, t)$ can be obtained from $R_1(z, t)$ and $R_2(z, t)$ as defined in Figure 4-2. They are given by:

$$R_1 = R_0 + \alpha \sin kz \cos \omega t \quad (4-6)$$

$$R_2 = -\frac{(1 + \alpha^2 k^2 \cos^2 kz \cos^2 \omega t)^{3/2}}{\alpha k^2 \sin kz \cos \omega t} \quad (4-7)$$

By substituting equations (4-6) and (4-7) into equation (3-11), the following expression for $\Delta\sigma(z, t)$ is obtained.

$$\Delta\sigma(z, t) = -\Delta P \cdot \frac{(1 + \alpha^2 k^2 \cos^2 kz \cos^2 \omega t)^{3/2} (R_0 + \alpha \sin kz \cos \omega t)}{\alpha k^2 \sin kz \cos \omega t \cdot \left(-\frac{(1 + \alpha^2 k^2 \cos^2 kz \cos^2 \omega t)^{3/2}}{\alpha k^2 \sin kz \cos \omega t} + R_0 + \alpha \sin kz \cos \omega t \right)} - \sigma \quad (4-7)$$

This is the interfacial tension fluctuation forced on the simulation.

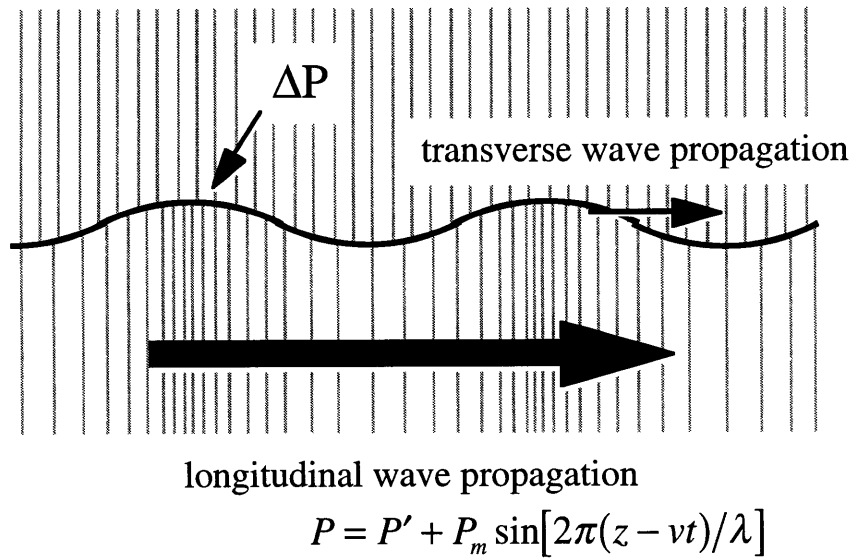


Figure 4-6 Propagation of a longitudinal wave creates a traveling pressure difference ΔP at the interface. The traveling ΔP creates a curvature which is essentially a traveling standing wave. Therefore, a transverse wave propagates in the same order of speed as a longitudinal waves propagates.

	Approx. t_b [timestep]	Average λ_m [lattice]	Growth Rate, q
theory	n/a	62.5	0.0029
simulation A	2200	50	0.0021
theory	n/a	62.5	0.00037
simulation B	10000	55	0.00032

Table 4-2 Typical results of capillary wave instability using the forced-perturbation scheme is compared with theoretical results. Theoretical growth rates are calculated using theoretical λ_m . The results show that the longer the t_b , the closer the growth rate and λ_m become to the theoretically predicted values.

Even with the forced standing wave disturbance scheme above, however, the fastest growing wave lengths obtained from simulations were shorter than the expected λ_m . More importantly, it was observed that the longer the time for thread break (t_b), the closer was the value of λ to the theoretical prediction as shown in Table 4-2.

4-4 Examination of Limitations of the Lattice-Boltzmann Method

From the above observations concerning the deviations of λ_m and the growth rate, the author first evaluated the viability of time scaling in the lattice-Boltzmann method for simulating capillary wave instability. Then the analysis was extended for some deficiencies caused by the discrete nature of the lattice.

In a real polymer, a sound wave propagates on the order of 10^3 m/sec [41]. A typical experimental thread breakup using polymers is conducted with diameters of 10^{-7} - 10^{-4} m and breakup times of $1 - 10^3$ sec [36]. This suggests that approximately 10^{10} oscillations of standing waves of wavelength λ_m have taken place before the breakup occurs.

In the lattice-Boltzmann simulation, however, sound propagates on the order of 1 lattice per timestep. Therefore, for a thread of 10 lattice units in radius to break up after 10^{10} oscillations of standing wave λ_m , 10^{12} timesteps are required. Unfortunately, this requirement is not feasible for simulation with current computing capabilities. In a typical capillary wave instability simulation, t_b was set between 500 and 2000 timesteps which implies there were only on the order of 10^1 oscillations of the standing wave before the breakup of the thread occurs. This poses a severe problem as shown in the example below.

Let R_0 be 6 lattice units, $\eta'/\eta=1$, and the interfacial tension be such that t_b is approximately 2000 timesteps. λ_m is expected to be 67 lattice units from theory. Since the speed of sound in 3D FCHC lattice-Boltzmann is approximately 0.7 lattice per timestep, the period of standing wave, $T_{osc} = \lambda_m/\nu$, is approximately 95 timesteps. The amplitude of the oscillation standing wave fluctuation α is given by equation (4-1), and is 6 lattice units when the thread breakup occurs ($t=t_b$). As shown in Figure 4-7, α_0 is approximately 0.8, and thus $q \approx 1 \times 10^{-3}$ timestep $^{-1}$.

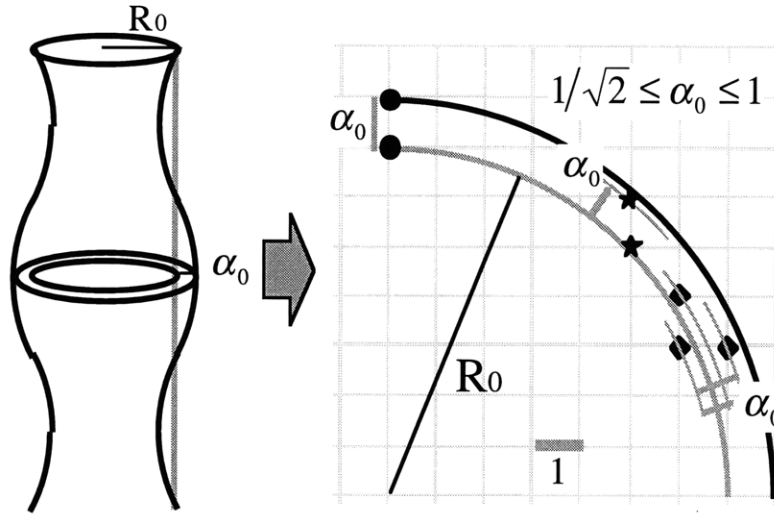


Figure 4-7 The minimum unit of α_0 on a discrete lattice is between $1/\sqrt{2}$ and 1.

In real life, millions of oscillations of the fastest growing standing waves take place before the thread breaks so that the growth of this standing wave is considered a continuous process. In the simulation with the above-described setting, however, there are only around 20 oscillations due to the long wave period with respect to t_b .

The linear perturbation theory predicts the growth of a wave's amplitude when the wave shape is applied to a cylinder [35]. However, when an oscillating standing wave occurs as a result of random noise, the growth of the wave's amplitude is achieved only when α_0 is positive with respect to the wave shape created on the thread, as illustrated in Figure 4-8. Therefore, the growth of the wave's amplitude can be discretized per oscillation of the standing wave. The discretized growth rate, q_d , is defined by:

$$q_d = \ln\left(\frac{\alpha}{\alpha_0}\right) / (\text{oscillations}) \quad (4-8)$$

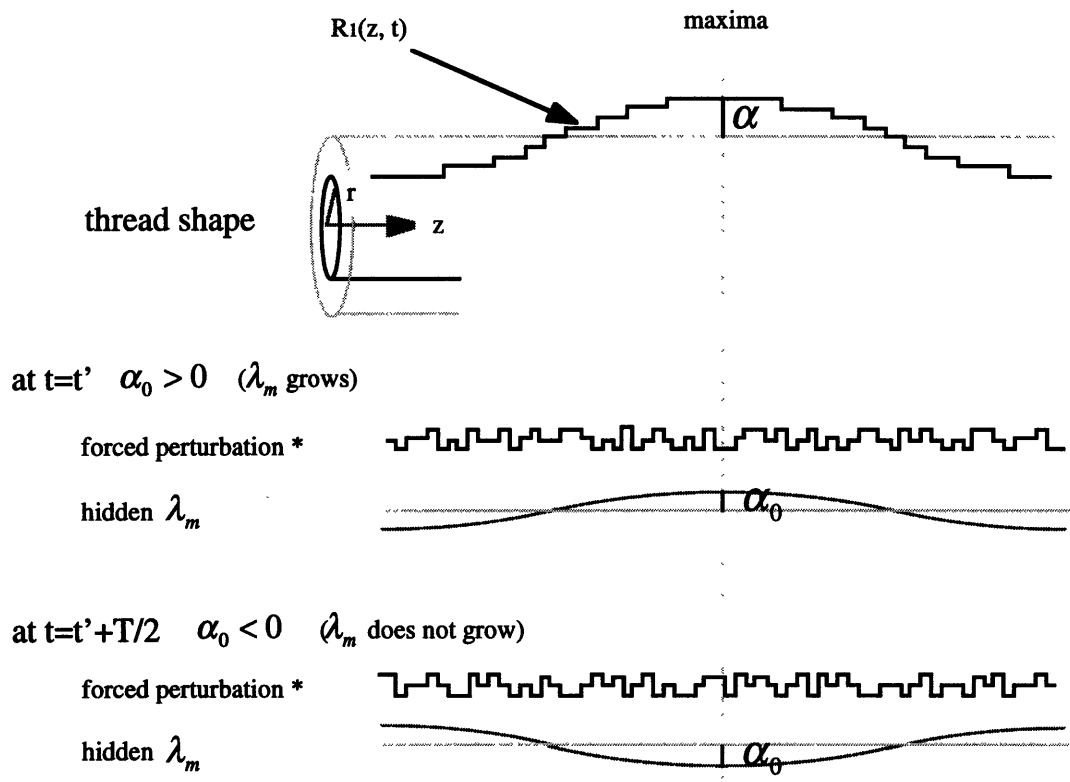


Figure 4-8 λ_m hidden in random forced perturbations oscillates at period T. Only when α_0 is positive with respect to the outline of the fastest growing wavelength (R_1), α grows due to instability.

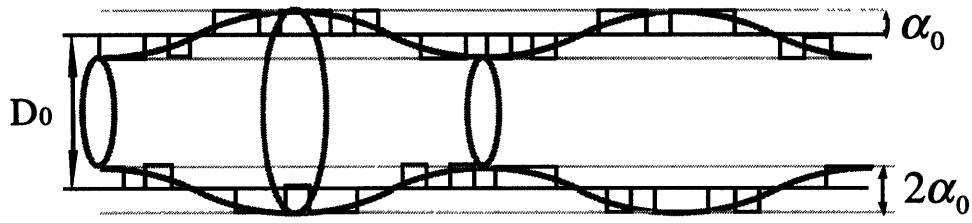


Figure 4-9 In order for the wave shape to be recognized in discrete space, the amplitude of the wave must become discretely larger than the amplitude of random noise. The drawing below illustrates the case when the amplitude of the wave becomes twice as large as the amplitude of the random noise.

In the given example, q_d is either 0.0959 or 0.0916 oscillation⁻¹ respectively since there can possibly be either 21 or 22 oscillations (with $\alpha_0 > 0$) depending on the initial phase of the standing wave.

In continuous space, the fastest growing wavelength outgrows the rest and establishes its wave shape gradually. Therefore, the amplitude of the wave's growth still counts when it is larger than that of the perturbation by marginal amount. In a discrete simulation, however, α has to become larger than the random noise level α_0 by at least 1 lattice unit to be recognized as a wave shape on the thread as illustrated in Figure 4-9. Suppose that α has to be twice as large as the noise amplitude, α_0 , in order to capitalize its wave shape on the thread (α_c), and define the time it takes for α to become $2\alpha_0$ as the shape capitalization time, or t_c . Since q_d can take either 1 or 2 values and the oscillation can start either at $\alpha_0 > 0$ or $\alpha_0 < 0$, there exists a gap between the earliest and the latest possible time for the shape capitalization. Such $t_{c,min}$ and $t_{c,max}$ are given by:

$$t_{c,min} = \left(\frac{\ln(2)}{q_{d,max}} - 0.5 \right) \cdot T \quad (4-10)$$

$$t_{c,max} = \left(\frac{\ln(2)}{q_{d,min}} + 0.5 \right) \cdot T \quad (4-11)$$

where T is the period of λ_m . One half is added or subtracted to take the initial phase of the wave into account. Natural log of 2 reflects the fact that α_c/α_0 is taken to be 2. In case for $\lambda_m = 67$ lattice units, $t_{c,min}$ becomes 637 timesteps and $t_{c,max}$ becomes 764 timesteps.

Figure 4-10 shows $t_{c,min}$ and $t_{c,max}$ at different λ_s . The latest possible time any wavelength capitalizes its shape on the thread is around 740 timesteps. However, by 740 timesteps any wavelengths between 52 and around 100 lattice units have a chance to capitalize their shapes on the thread.

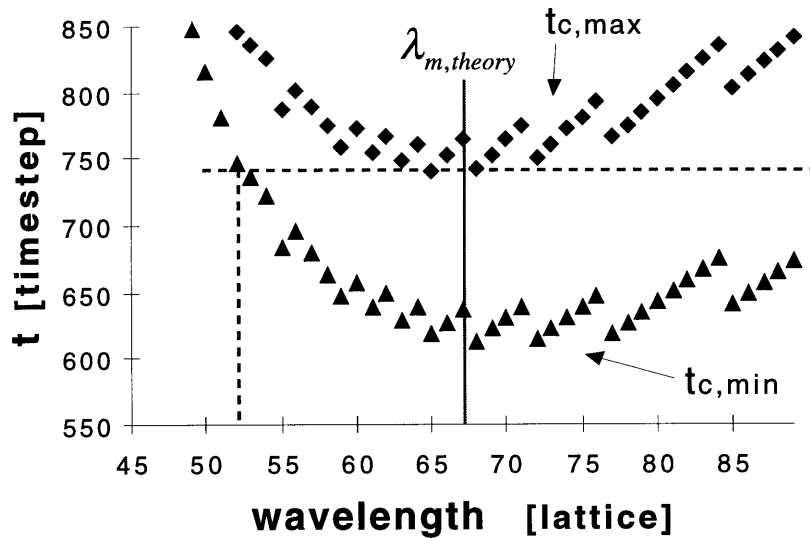


Figure 4-10 The time for wave shape capitalization for the case $t_b=2,000$ timesteps is shown with respect to various wavelengths. Any wavelengths between 52 and around 100 lattice units (not shown in the figure) have a chance to capitalize their wave shapes, since $t \approx 740$ is the latest possible time wavelengths of 66 and 68 can capitalize their shape. A gradual increase in t_c between $\lambda=72$ and 76 lattice units is due to the same discretized growth rate, but the longer period of oscillation. A sudden jump of t_c between $\lambda=76$ and 77 lattice units is due to a sudden increase in the discretized growth rate. This is because the increase in the standing wave period enables one less oscillation before the thread breaks.

The possibility of too many wavelengths having chance to capitalize their shape can be reduced, but at a cost of computing time. Figure 4-11 shows the case when t_b is set at 20,000 timesteps while lattice dimensions, cylinder radius, viscosity ratio are kept the same. At this growth rate, potential wavelengths that can capitalize their shapes are narrowed down to between 61 and 74 lattice units. As shown in Figure 4-12, when growth rate is decreased so that $t_b=200,000$ timesteps, the range is further narrowed down between 65 and 69 lattice units with the fastest growing wavelength predicted at 67 lattice units, as forecasted by the theory.

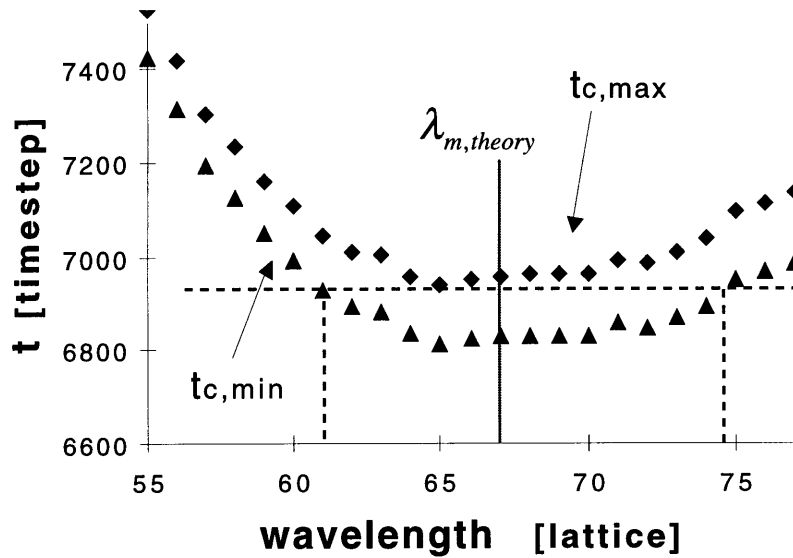


Figure 4-11 The time required for wave shape capitalization for the case $t_b=20,000$ timesteps is shown with respect to various wavelengths. The range of wavelengths that can potentially capitalize their wave shapes is narrowed down to between 61 and 74 lattice units.

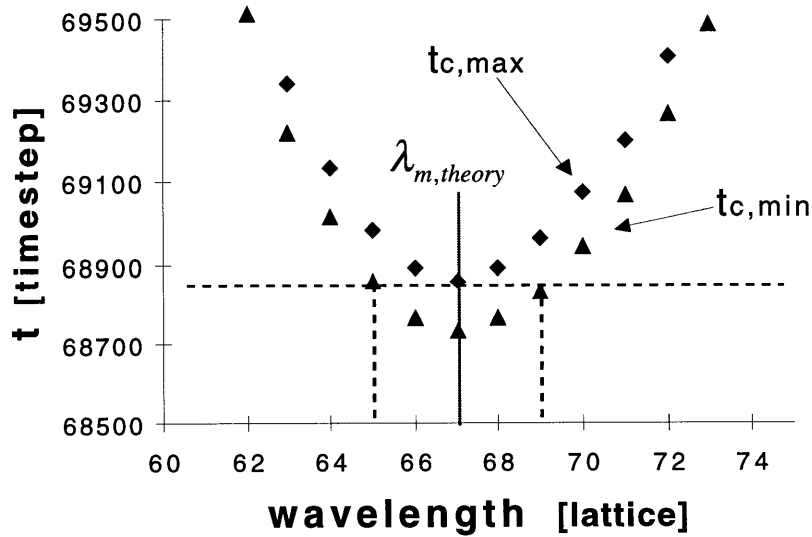


Figure 4-12 The time required for wave shape capitalization for the case $t_b=200,000$ timesteps is shown with respect to various wavelengths. The range of wavelengths that can potentially capitalize their wave shapes is further narrowed down to between 65 and 69 lattice units.

Increasing t_b is essentially an attempt to smooth the discretized effect of the growth rate and to decrease the ratio of the oscillation period to t_b . It is, in fact, an attempt to make the simulation closer to the real life situation.

In real life, α_0 can also be taken to be arbitrarily small and there is no such a thing as a shape-establishing amplitude because the space is continuous. Since the effort to extend the simulation size in time domain increased the accuracy of the simulation, one may consider extending the simulation in the spatial dimension in order to make the relative size of α_0 small with respect to α_c . However, extending the simulation in the spatial domain does not improve the situation readily because the period of a oscillating standing wave is directly proportional to the radius of the cylinder as shown in equation (4-12) and (4-13) below:

$$T_{osc} = \frac{\lambda}{v} \quad (4-12)$$

$$\lambda_m = D_0 \Phi(\eta'/\eta) \quad (4-13)$$

where $\Phi(\eta'/\eta)$ is a function plotted in Figure 4-3. Figure 4-13 shows the case for $R_0=60$ lattice units and $t_b=200,000$ timesteps. In addition to the fact that the time and memory requirements for running a simulation of this size and length are prohibitively expensive, the selectivity of the fastest growing wavelength is not improved at all. This is one of the limitations of the lattice-Boltzmann method, originating from its inflexible wave propagation speed.

In a continuous system, a standing wave of the wavelength λ_m simply grows continuously gradually until the thread breaks. In discrete systems such as the lattice-Boltzmann simulation, however, the growth of α is also discrete, as discussed above. This causes another potential defect in the simulation. Even if any wavelength has

successfully capitalized its wave shape according to the previously given definition, disturbances as large as half of its established wave amplitude α_c will continuously influence the capitalized shape. The relative size of the large random disturbance α_0 can be decreased only after α discretely increases its size further. Until then, the capitalized wave shape is prone to disturbances of other wavelengths that could slow down the growth of the capitalized wave shape by obscuring its shape, or even destroy the shape altogether. From this stand point, increasing R_0 will decrease the relative size of α_0 and allow longer growth time when $\alpha_0 \ll \alpha$. Although increasing R_0 will multiply the cost of simulation in terms of both memory requirement and computation time very quickly, the effect of destructive disturbances by the other wavelengths may be reduced and the wave may achieve a growth rate very close to the theoretical value if the simulation is indeed conducted. Unfortunately, this predicted trend has not yet been confirmed.

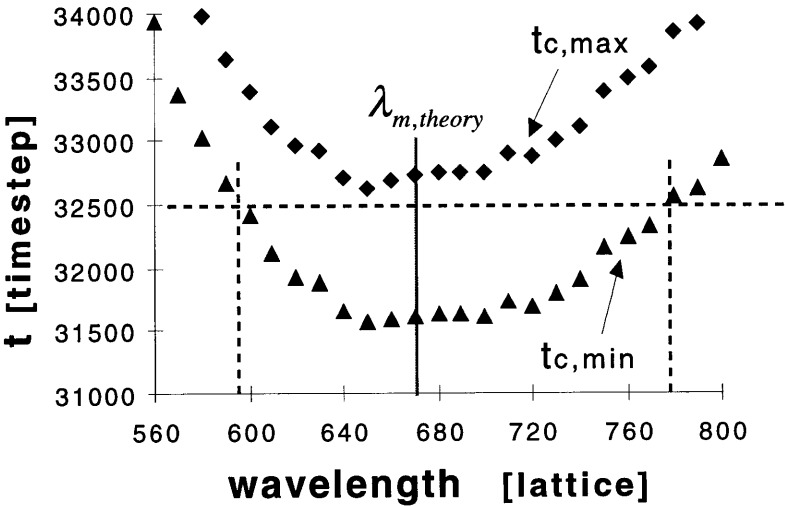


Figure 4-13 The time required for the wave shape capitalization for the case $t_b=200,000$ timesteps and $R_0=60$ lattice units is shown with respect to various wavelengths. When compared to Figure 4-9, the spatial dimension was increased by 10 order of magnitude (and simulation length by 100-fold), but the accuracy of the fastest growing wave length obtained from the simulation does not improve. Increase in the initial radius of the cylinder just costs more computational time and memory.

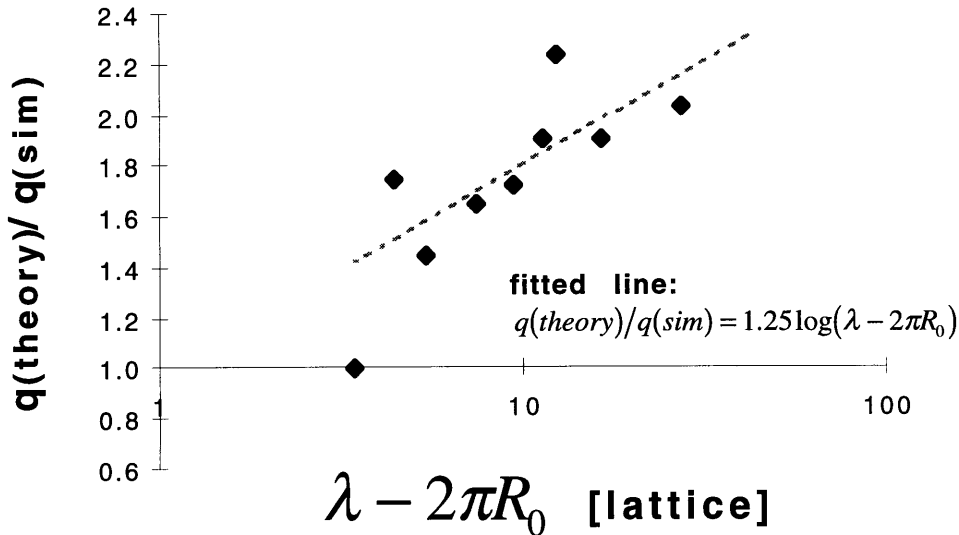


Figure 4-14 Since wavelengths longer than the circumference are unstable and grow, the longer the wavelength, the more obstructing disturbances they encounter from shorter wavelengths. The degree of obstructing disturbances a wavelength receives (modified wavelength) is approximated by the wavelength minus the circumference. In simulations, the shorter the wavelength, the less obstructing disturbance it receives on a discrete lattice so that it can grow near its natural growth rate. Data for this figure comes from plural numbers of capillary instability experiments with $t_b \approx 1,000$ timesteps and $R_0 = 5.5$. The rest of the parameters for the simulations may vary.

In the simulations, the growth rate is generally found to be smaller than the expected value for the given wavelength observed. Although further investigation is required, it is observed that the shorter the thread-breaking wavelength, the closer its growth rate is to the expected value as shown in Figure 4-14. This observation implies that longer wavelengths are more prone to the growth obscuring disturbances and are therefore harder to grow. Figure 4-14 is created from various capillary wave instability experiments with $t_b \approx 1000$ timesteps and $R_0 = 5.5$ lattice units. The data spread in $\lambda - 2\pi R_0$ is expected to converge to $\lambda_m - 2\pi R_0$ as t_b becomes larger.

The expected t_c was recalculated for each wavelength using the adjusted growth rate, $q_{adj} = q_{theory} / 1.25 \log(\lambda - 2\pi R_0)$. Figure 4-15 shows the recalculated time for the wave capitalization for the case of $t_b=2,000$ timestep. The figure shows the shift of the quickest capitalization wavelength from 67 to 55. Wavelengths of around 55 were observed for breakup in the simulations. No correlation between the deviation of growth rate and breakup time has been confirmed.

Simulation of capillary wave instability elucidates some limitations of the lattice-Boltzmann method in both the time and physical dimensions.

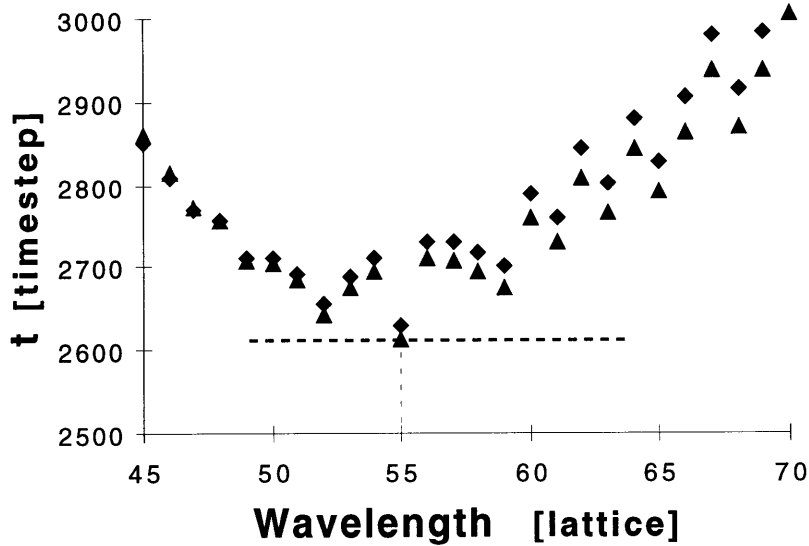


Figure 4-15 The case for Figure 4-7 is re-plotted using the new expected simulation growth rates based on the fitted line shown in Figure 4-10. Note that the wavelength for the shortest t_c shifted from 67 to 55 [lattice]. t_c increased over all due to the effect of destructively interfering disturbances of competing wavelengths.

5. Applications

5.1 Introduction

The ultimate goal of this research is to faithfully reproduce complex flow situations, such as breakup and coalescence of moving phase domains, observed in polymer processing using computational simulations, (In this thesis, the term “breakup” refers to the actual breakup of a droplet into two separate domains unless otherwise noted.) For experimental investigation, previous researchers have used the four roller device shown in Figure 5-1 to produce various droplet-breaking flows. The analytical expression for flows created by the four-roller device [42] is given by:

$$\bar{v} = \bar{L} \cdot \bar{r} \quad (5-1)$$

where

$$\bar{L} = \frac{\dot{\gamma}}{2} \begin{bmatrix} 1 + \varepsilon & 1 - \varepsilon & 0 \\ -1 + \varepsilon & -1 - \varepsilon & 0 \\ 0 & 0 & 0 \end{bmatrix} \quad (5-2)$$

ε takes values between -1 and 1. Since a droplet tends to rotate without breaking up when $\varepsilon < 0$, experiments are usually conducted with $\varepsilon \geq 0$. The locations where the most breakups are believed to occur in processing equipment is at the tip of rotor blades of a batch mixer or the tip of the kneading blocks in a twin-screw extruder. At these locations, flows are neither purely extensional ($\varepsilon = 1$) nor simple shear ($\varepsilon = 0$), but rather a combination of both. However, for analytical and experimental convenience, simple shear and pure extensional flows are commonly investigated.

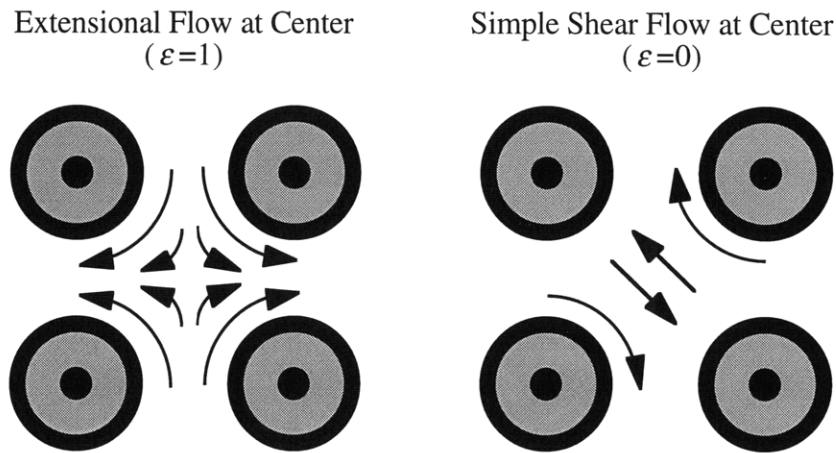


Figure 5-1 Four-roller device.

The capillary number, a ratio of the viscous droplet breakup forces to interfacial stabilization forces, is used as a measuring stick for breakup. The critical capillary number, Ca_{crit} , is defined as the capillary number beyond which a droplet begins transient elongation [43]. Although transient elongation does not directly imply the breakup of a droplet, breakup of the elongated droplet has been observed to occur near this Ca_{crit} value by several mechanisms, depending on the viscosity ratios and type of flow. The critical capillary number is analytically predicted by Barthés-Biesel and Acrivos [44] with their $O(Ca^2)$ theory and by Bentley and Leal [45] with their slender body theory for very small values of the viscosity ratios. Experiments by Stone using the four roller device show good agreement with theory at various viscosity ratios and for various flow types signified by various ϵ s, as illustrated in Figure 5-2. As shown in the figure, extensional flow ($\epsilon=1$) is more effective in breaking up droplets than simple shear flow ($\epsilon=0$) since it does not allow the droplet to rotate. In simple shear flow, the $O(Ca^2)$ theory predicts that no breakup of a droplet will occur when the viscosity ratio exceeds 3.6. Experimentally, no breakup was

observed above a viscosity ratio of 3.5 [46] and 6.0 [31] in work performed by two different experiments.

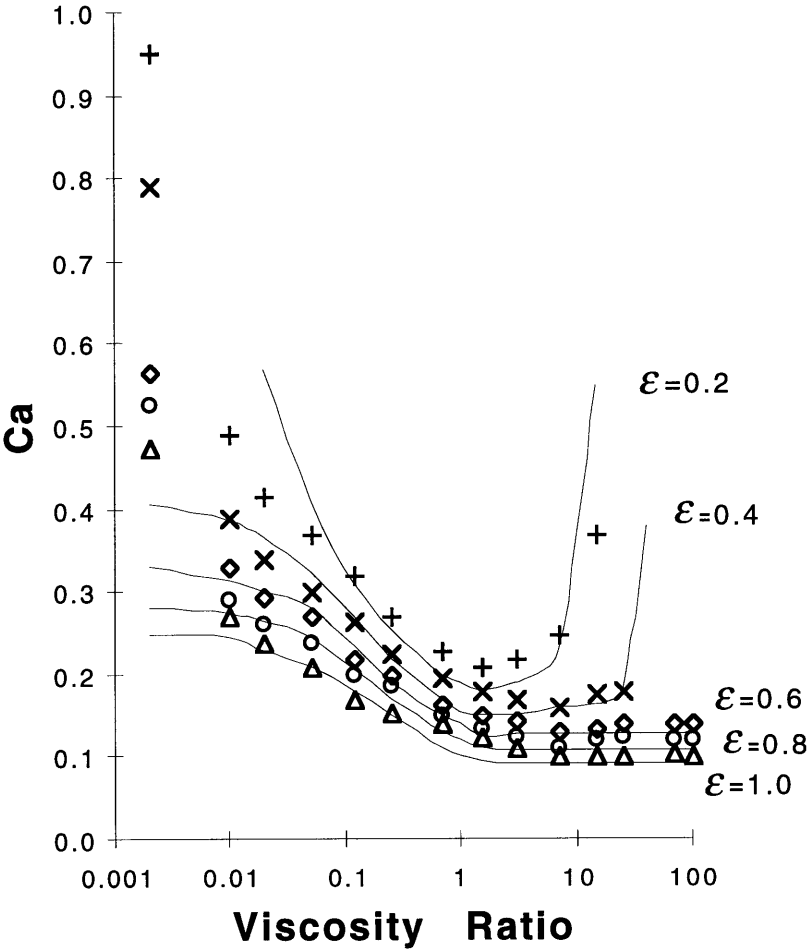


Figure 5-2 Effect of the type of flow on the critical capillary number for droplet breakup. The solid line is $O(Ca^2)$ theory [44] and the data points are experimental data generated by Stone [43].

In polymer processing, irregularly shaped blades or kneading blocks are rotated to create various droplet breaking flows. Naturally, the stress exerted on a droplet is not

constant, whether extensional or shear in nature. For example, the stress around a droplet increases when a blade is approaching and decreases when the blade is receding. In single-screw extruder, the flow circulates between a high shear region near the barrel and a low or no shear region in the middle or bottom of the channel of the screw [33]. Droplet breakups also occur, sometimes more effectively, at these transient locations where the stress exerted on a droplet is not at its maxima. When a highly elongated droplet is suddenly placed in a no-stress condition, both ends of this elongated cylinder form a bulbous shape. Depending on the initial elongated shapes and the viscosity ratios of the dispersed and matrix phases, either the neck of the bulbous ends pinch-off or the bulbous ends coalesce. A series of comprehensive experiments, computational simulations and intuitive analysis for this type of breakup was done by Stone, Bentley and Leal [32, 47].

While some droplets are broken into smaller ones, many smaller droplets meet and coalesce with each other, especially when the volume ratio of the droplet phase becomes sufficiently high. After a long enough mixing time, a steady-state average droplet size will be reached which is representative of equilibrium between breakup and coalescence. When two droplets coalesce in an head-on collision, flattening of the moving fronts of the droplets occurs first. As the flattened circular plates of the droplet fronts approach each other, a sheet of the fluid in between is drained and becomes thinner. Once the thickness of the film reaches a critical thickness, the film ruptures and droplet coalescence takes place [48]. Understanding the details of the mechanism of thin film rupture is of major interest because of its role in the coalescence phenomena at the mixing equilibrium. Unfortunately, most theoretical and experimental investigations have been conducted for the coalescence of a droplet approaching a horizontal interface due to gravity [49], rather than head-on collisions of two droplets due to flow. Since most polymers are highly viscous, gravity is not an important factor in their blending. Unlike a droplet colliding with a flat interface due

to gravity, droplet collisions induced by a flow may not always result in coalescence. Either bouncing back or rotation may occur, if the film in between them does not drain fast enough as illustrated in Figure 5-3. Due to the complexity of the coalescence mechanism, no single analytical model accurately illustrates the thinning of the film between the droplets. However, these models offer approximate relationship between hydrodynamic parameters and the film thinning. For example, the larger the radius of a droplet, the smaller the rate of film thinning [50]. Among the few experiments of coalescence by head-on collision, Scheele and Leng [48] found that the phase of the droplets oscillations, rather than their approaching velocity, was the factor which controlled of whether the injected droplets coalesce or bounce. Their observation was confirmed by Jeelani and Hartland's [51] analytical model.

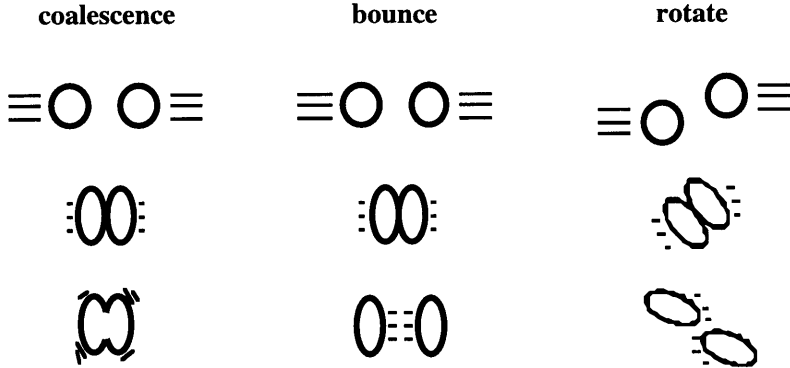


Figure 5-3 Three modes of collisions when two droplets of equal size approach each other.

Understanding the macroscopic effects of coalescence is also important in polymer processing. The average radius of a droplet is expected to increase as the concentration of dispersed phase increases due to coalescence. Prediction of the increase of the equilibrium droplet size requires an understanding of collision and coalescence probabilities upon

collisions. Collision probability has been modeled satisfactory using the idea of population balance [52]. However, the coalescence probability upon collision is not well understood, even for a Newtonian fluids, due to the complexity involved in the film thinning process [53]. Sundararaj and Macosko [54] have experimented with the effect of the concentration in polymer blend coalescence using twin-screw extruders and a batch mixer. They found that the average droplet diameter increased as the concentration of the dispersed phase increased.

In this thesis, breakup and coalescence events are simulated using the 3D lattice-Boltzmann method, and are compared with analytical models and experimental results.

5.2 Breakup in Simple Shear Flow vs. Capillary Number

Breakup of a droplet in shear flow using the 2D lattice-gas automata was first simulated by Rothman [12]. In spite of its difficulty of implementation, droplet breakup in shear flow was also observed using the 3D lattice-gas automata [55]. In the lattice-Boltzmann simulation, however, it is harder to observe physical breakup because the method does not have the implicit noise or disturbance that help its lattice-gas counterpart to break. To produce real-life situation, an appropriate level of noise can be added by the methods described in the capillary wave instability section of this thesis, however.

While there is not yet a clear-cut analytical model to describe the mechanism of physical droplet breakup in a stress field, analytical work has been done to predict the point at which the droplet shape is no longer in equilibrium. According to Barthés-Biesel and Acrivos [44] who use linear stability theory to analyze droplet breakup, a droplet starts elongating, then it breaks once the point where no steady analytical solution exists is passed. This point is called the analytical breakup point. This turns out to be a function of

the capillary number and the ratio of the viscosity of the dispersed and the matrix phase, η'/η .

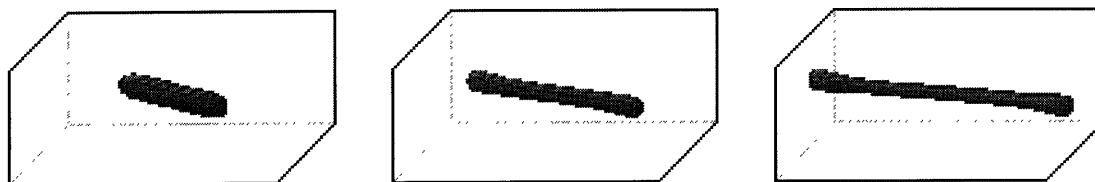


Figure 5-4 When the capillary number reaches its critical value, a droplet begins its continuous elongation.

Continuous elongation of a droplet, followed by its physical breakup, is observed in the lattice-Boltzmann simulations, once the capillary number reaches a critical value as shown in Figure 5-4. The capillary number at this state is defined as the critical capillary number, Ca_{crit} .

In simulations, the capillary number was manipulated by changing the interfacial tension rather than the shear rate. Since the theory and experimental results of droplet breakup are expressed as a relation between Ca_{crit} and η'/η , this method does not obscure the accuracy of results obtained from the simulation. The interfacial tension was initially set high, and was then gradually decreased until the elongation of the droplet was observed near Ca_{crit} . At each modification of the interfacial tension, the simulation was run long enough time so that the droplet reached its equilibrium shape at any given capillary number and η'/η .

Simulations of droplet breakup in simple shear using the lattice-Boltzmann method were conducted with a 100 (or 150)x40x40 lattice and a droplet radius of 7 lattice units.

The viscosity ratios of 1 and 0.01 were used to observe the breakup shape and qualitatively compared with the experimental breakup shape seen by Torza, Cox and Mason [56]. The same perturbation method chosen for capillary wave instability simulations were applied. As shown in Figure 5-5, the lattice-Boltzmann simulation results and the experimental results roughly agree.

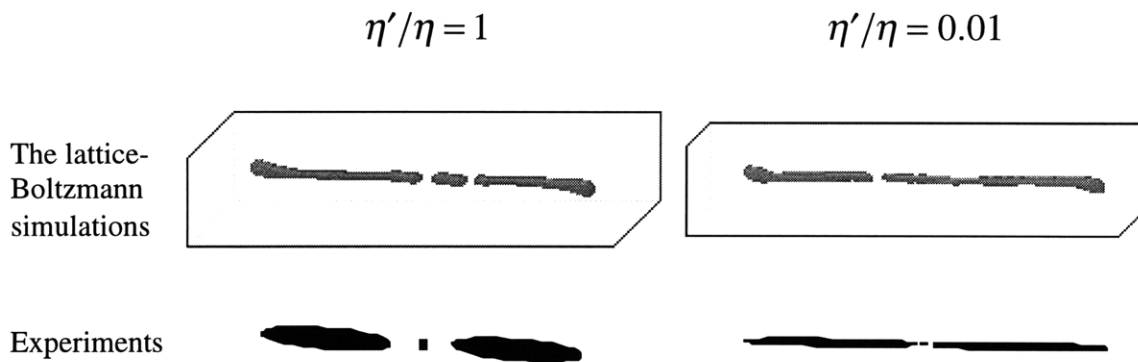


Figure 5-5 Shapes of the droplet at breakup in simple shear flow using the 3-D lattice-Boltzmann method are compared with the shape observed in experiment by Torza, Cox and Mason [56]. The drawings for the experiment are sketched by the present author from the published pictures.

As a semi-quantitative test, $\eta'/\eta = 10, 3, 1, 0.3, 0.1,$ and 0.01 were used to find Ca_{crit} and were compared with Barthés-Biesel and Acrivos's [44] theoretical results and experimental results by Torza, Cox and Mason [56] and also by Grace [46]. These experimental results were reproduced from the author's reading of published figures. As shown in Figure 5-6, results from the simulations agree well with experimental results at $\eta'/\eta = 0.1, 0.3,$ and $1,$ considering the wide distribution of experimental results. They

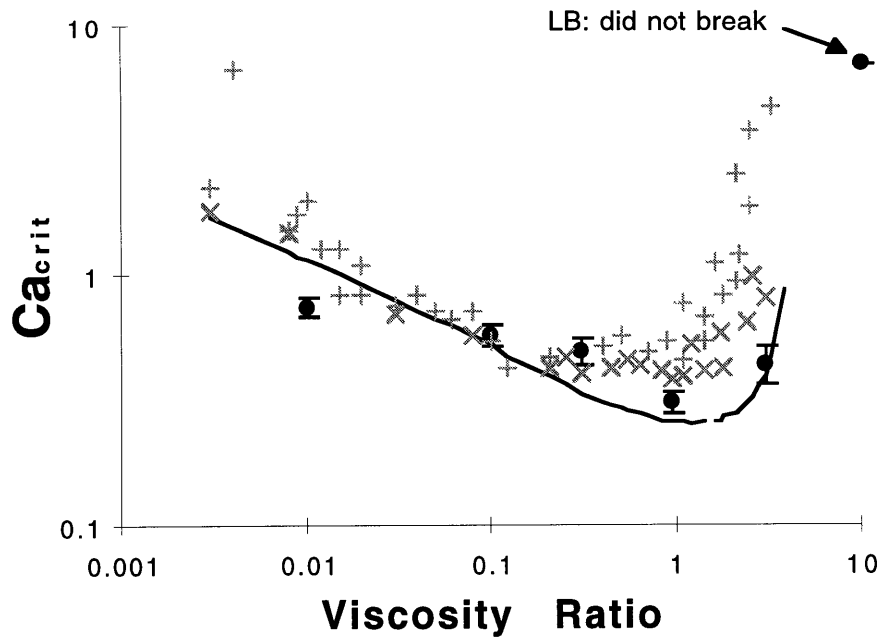


Figure 5-6 Critical capillary numbers measured at different viscosity ratios are plotted. •, +, x, and – indicate results from the lattice-Boltzmann simulations, Grace’s [46] experiments, Torza, Cox and Mason’s [56] experiments and Barthés-Biesel and Acrivos’s [44] analytical work, respectively.

also agree well with the theoretical results at those viscosity ratios and also at $\eta'/\eta = 3$. No breakup was observed at $\eta'/\eta = 10$ as predicted by theory and experiments. At this viscosity ratio, a droplet simply keeps rotating and does not stretch, as shown in Figure 5-7. A large deviation between theory and experimental results is observed at $\eta'/\eta = 0.01$. This deviation is believed to be caused by limitations of the lattice dimensions used for the simulations. A stable droplet shape in a simple shear flow is maintained due to a circulating flow within the droplet. However, when the breadth of the elongated droplet becomes approximately 2 lattice units, this circulatory flow becomes impossible and the droplet becomes unstable. The predicted shape of the droplet before it breaks at $\eta'/\eta = 0.01$ is much narrower than that of higher viscosity ratios and hence, has a greater chance of

reaching this limit. Therefore, at $\eta'/\eta = 0.01$ the absence of this internal flow allows a droplet to be dragged by the shear flow and enhances the droplet elongation, causing premature rupture even if the droplet has not reached its true Ca_{crit} . Further investigation is required using a larger lattice size for more accurate measurements of the Ca_{crit} in the lattice-Boltzmann method.

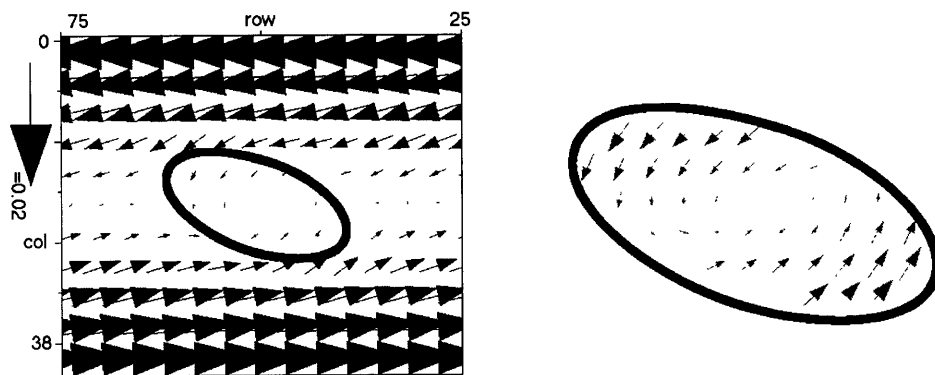


Figure 5-7 A 2D slice of a droplet's velocity profile. The figure is drawn at viscosity ratio of 10 and a capillary number of 7. The droplet simply rotates instead of breaking up.

5.3 End-pinching

Stone, Bentley and Leal used the four-roller device shown in Figure 5-1 to extensionally elongate droplets to study end-pinching in their experiments. When the capillary number reached its critical value due to increases in the shear rate, the droplet began its continuous elongation. The flow was halted when the elongation reached a certain extension ratio, L/a , defined in Figure 5-8. Shapes of the elongated droplet when the flow is stopped depend on the viscosity ratios and are shown in Figure 5-9. They

observed that the droplet either relaxes back to a spherical shape or the droplet breaks up at both ends, depending on the degree of initial elongation and η'/η . The breakup/no-breakup relation is plotted as the elongation ratio versus η'/η and is shown in Figure 5-10. Just as with breakup in strong shear, breakups of this nature occur most easily in the range $0.1 < \eta'/\eta < 1$.

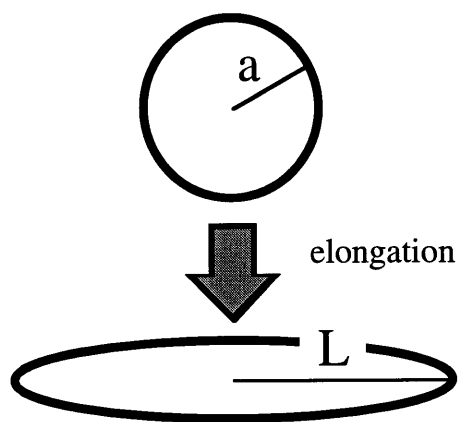


Figure 5-8 Definition of degree of elongation, L/a . The initial sphere of radius a elongates and becomes a spheroid with a length L .

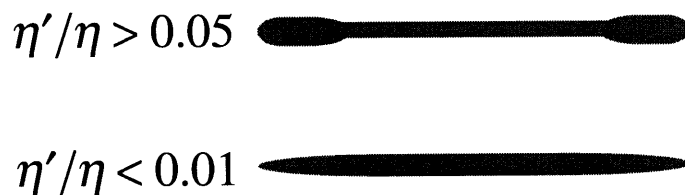


Figure 5-9 Elongated droplet shape at different viscosity ratios.

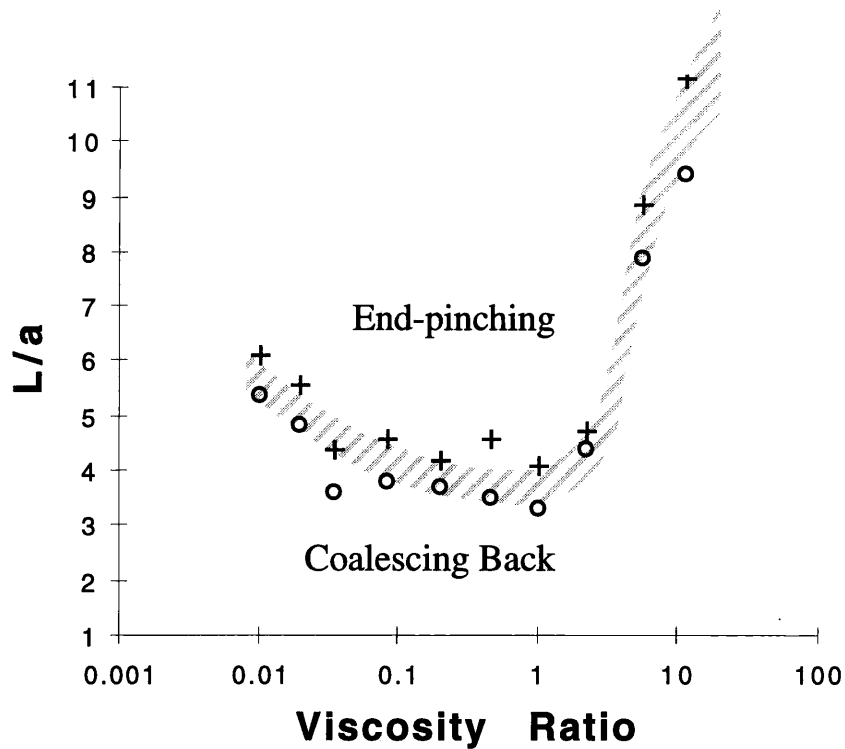


Figure 5-10 Experimental results of end-pinching/coalescing-back of the droplet at various elongation ratios and viscosity ratios are plotted [32]. + indicates the conditions at which end-pinching occurred and o indicates the conditions at which the coalescence of two bulbous ends occurred.

Although droplets in these experiments are highly elongated and have a cylindrical shape except at the ends, the breakup mechanism observed from Stone, Bentley and Leal's [32] experiment is entirely different from that of capillary wave instability. In their experiments, the inflated ends of the elongated sphere break off from the rest of the body due to capillary pressure variations, rather than due to the growth of small random disturbances which occurs in capillary wave instability. Stone, Bentley and Leal call this breakup phenomenon "end-pinching."

The time it takes for end-pinching is usually much shorter than that for the growth of capillary waves. Unless the elongation ratio L/a was very large, no capillary wave instability was observed in their experiment because of this time difference. Experimentally, the time it takes for the cessation of the flow after the rollers are halted is much shorter than the time it takes for end-pinching. Using this fact, Stone, Bentley and Leal [32] placed a stress-free elongated droplet of a shape similar to what is shown in Figure 5-9 into a quiescent matrix for their computational simulation in order to analyze the mechanism of end-pinching. Using the boundary-integral method, they have quantitatively reproduced earlier experimental results of end-pinching.

The reason for end-pinching's dependence on η'/η is has also been analyzed by Stone, Bentley and Leal. At low η'/η , internal flows in the droplet phase move from the narrow cylindrical mid-section to the bulbous ends due to the pressure gradient. The bulbous ends too move toward each other due to interfacial tension, but do so slowly due to the viscosity of the matrix phase. The flows near the bulb move quickly into the ends, making their original location scarce of fluid and creating necks at these locations. These necks are then broken due to a capillary pinch-off. At high η'/η , however, the flows within the cylindrical part move slowly while the bulbous ends approach each other more quickly due to the lower relative matrix viscosity. Therefore, at high η'/η , there is a greater chance for the two ends to coalesce back into one piece.




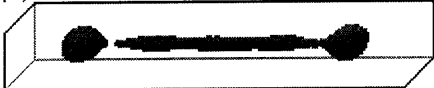




	lattice-Boltzmann method [timestep]	experiment [sec]	boundary integral method [sec]
$\eta'/\eta = 1$			
	0	0	0
	1500	1	48
	2500	n/a	77
	3500	2.6	100
$\eta'/\eta = 10$			
	0	0	0
	17000	5	173
	30000	12	396
	50000	15.3	600

Figure 5-11 3D renderings of the lattice-Boltzmann simulations and the times it takes to form each respective shape are shown in the first two columns. The author compared the published experimental and the simulation (the boundary integral method) results [32, 45] to the figures in the first column, and estimated the time evolution of their results in the third and fourth columns.

In the lattice-Boltzmann method, a 200x28x28 lattice was used to simulate the end-pinching phenomenon. The simulations were focused in the range of $0.1 < \eta'/\eta < 10$ so that the initial shape of the stress-free elongated droplet had bulbous ends whose breadths were twice as large as that of the middle section. Figure 5-11 illustrates an opaque gray elongated droplet in a box of clear matrix phase. The elongation ratio L/a was chosen as approximately 8.6, the same ratio as Stone and Leal's simulation. The viscosity ratios of

0.1, 1, and 10 were used to compare these simulations with the previous experimental and computational results.

In four-roller experiments, the time it takes for the cessation of the flow is approximately 1/5 the time it takes for end-pinching, and 1/50 the time it takes to recover to its spherical shape in cases where no breakup occurs. In these lattice-Boltzmann simulations, the cessation of the flow for the lattice size used occurs around 500 timesteps for the matrix viscosity used. Therefore, the interfacial tension was chosen so that the time for end-pinching occurs around 5,000 timesteps. Since the expected time for the breakup due to growth of capillary waves at this interfacial tension is on the order of 50,000 timestep, only the breakup/no-breakup due to end-pinching was observed during the simulation.

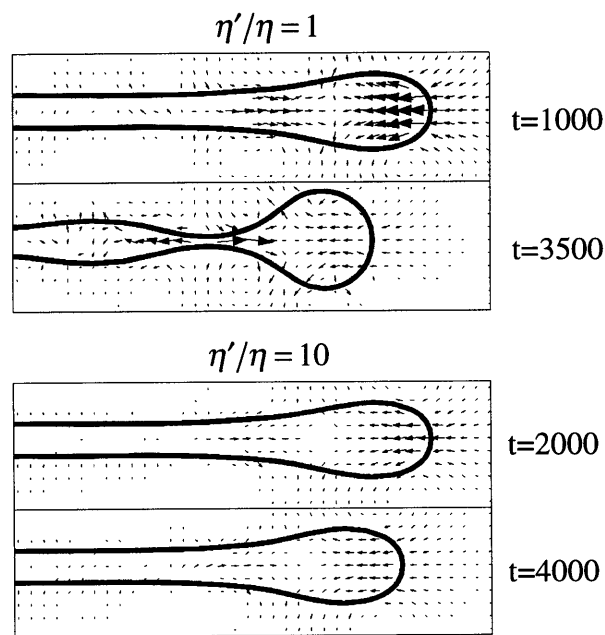


Figure 5-12 2D projection of the velocity vector plots of 3D lattice-Boltzmann simulations at two viscosity ratios are shown. Arrows represent velocity vectors in the flow.

Typical end-pinching breakup and coalescence of two bulbous ends were simulated by the lattice-Boltzmann method and are shown in Figures 5-11 (3D rendering) and 5-12 (velocity vector rendering). In the simulations, breakup by end-pinching was observed at $\eta'/\eta=0.1$ and 1, while the elongated droplet shrank back to a spherical shape when $\eta'/\eta=10$. These results agree with the previous experimental and computational results. The evolution of the droplet shape in time also agrees fairly well with the previous experimental and computational results, as shown in Figure 5-11. However, further investigation using intermediate η'/η s and different initial elongation ratios is being pursued to ensure the simulation's quantitative accuracy in reproducing end-pinching.

5.4 Coalescence of a Doublet

In the standard lattice-Boltzmann simulation and the lattice-fluid automata implementation, the local color gradient \vec{f} is given by the equation (4-3). This vector points in the direction where the probability of finding red particles is the highest and the probability of finding blue particles is the lowest. This implementation, however, assumes that only one interfacial boundary exists at a single lattice point, and does not correctly reflect the case where two interfaces are approaching each other within the lattice point, as illustrated in Figure 5-13.

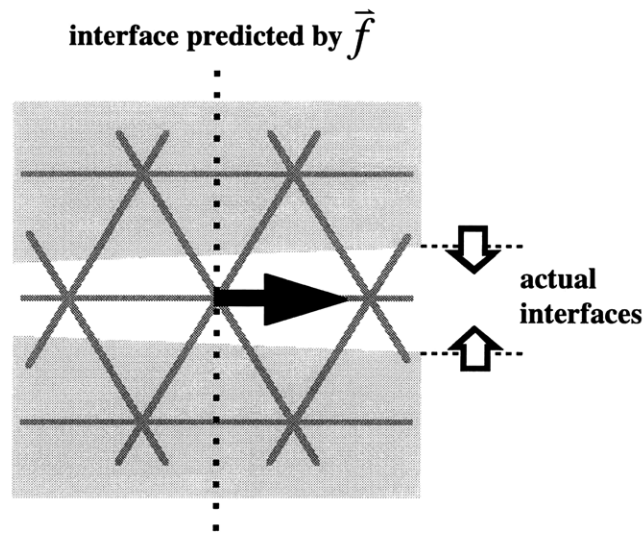


Figure 5-13 With the conventional color separation scheme for the lattice-Boltzmann method, the direction of the interface cannot be correctly defined when two phase boundaries approach within a single lattice unit.

Coalescence is an event where two interfaces approach and merge into a single interface when the distance between the interfaces reaches a critical thickness [49]. In lattice-Boltzmann simulations using the standard color separation scheme based on equation (4-3), this critical thickness is expected to be approximately 1 lattice unit because the simulation technique cannot correctly recognize the direction of the interface and separate colors, and therefore a continuous phase becomes discontinuous as two interfaces approach within a single lattice. This inscalable critical thickness of the simulation poses a serious limitation when simulating a coalescence event.

In real-life situations, the critical thickness of a film before it breaks is on the order of 500 Å [57]. Therefore, this thickness should be set equal to 1 lattice unit to correctly scale the coalescence phenomena when using the lattice-Boltzmann method. If this scaling rule is used, however, a simple simulation case such as a doublet collision requires at least

a 450x120x120 lattice since the typical equilibrium size of droplets in a polymer blend is on the order of 1 μm . A 450x120x120 lattice requires computational memory on the order of Giga-bytes and prohibitively long computational times per single time evolution even with the fastest current computers. Therefore, with the existing color separation scheme and the current computational power, it is impossible to correctly simulate a complex hydrodynamics case such as multiple droplet breakup and coalescence, at which the lattice-Boltzmann method is supposed to excel.

To examine the quantitative accuracy of the lattice-Boltzmann simulation of coalescence, Scheele and Leng's [48] experiment is chosen as a benchmark. In their experiment, they injected two equal size droplets of anisole simultaneously toward each other at the same velocity in water. They found that the probability of coalescence is not an obvious function of the drops' impact velocity, but is sensitive to the phase of oscillations of the droplets at the point of contact. The phase angle used here is defined in the Figure 5-14. They observed coalescence in the experiment only when the droplets have a phase angle between 0° and 135° . Their observation is supported theoretically by Jeelani and Hartland [51].

A lattice of 150x40x40 or similar size was used in the lattice-Boltzmann simulation. Two droplets of opposing velocity were placed at ends of the lattice in a quiescent matrix and were allow to collide with each other. The interfacial tension, viscosity and initial approaching velocity were carefully chosen to scale Scheele and Leng's experimental setting. The initial distance between the two droplets was also varied in order to create various phase angles. Although dozens of simulations were conducted, all of them resulted in complete coalescence and no bounce back was observed as summarized in Figure 5-14. The author concluded that this observation was due to limitations of how the lattice-Boltzmann method handles the color separation at the phase domain.

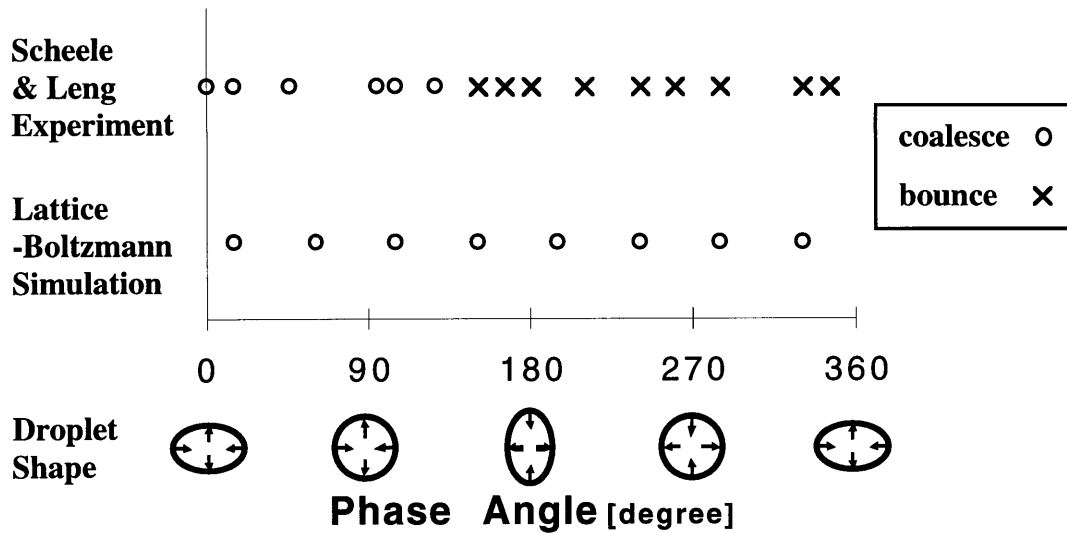


Figure 5-14 Results of coalesce/bounce for experiments by Scheele and Leng and of the same experiment simulated the lattice-Boltzmann method are summarized. Two simultaneously injected droplets move toward each other as their shapes oscillate as shown below. Whether a droplet bounces or coalesces correlates to the range of phase angles in the oscillations. The droplet moves in horizontal direction.

To improve the lattice-Boltzmann simulation in case of coalescence, a modification to the standard lattice-Boltzmann color-separation scheme was introduced. This modification theoretically improves the handling of the phase domains at the lattice points. The concept and its implementation are first described, followed by descriptions of the qualitative testing of the simulation using the modified code.

To simulate the droplet breakup and coalescence within a reasonable lattice size, the critical thickness for the film breakup has to be smaller than 1 lattice unit. There are four steps to set the critical thickness less than unity. The first two steps are to recognize when two interfaces approaches within a single lattice point and to correctly calculate the direction of the interface. Once the model distinguishes the case of the local lattice point having two interfaces, the next step is to measure the thickness of the matrix, or continuous phase at the lattice point. The final step is to separate the phases in the correct manner. When the

thickness of the matrix is thicker than the specified critical thickness, the phases are separated so that two interfaces are preserved, and when the thickness is below it, only one interface is created as a result of the color separation.

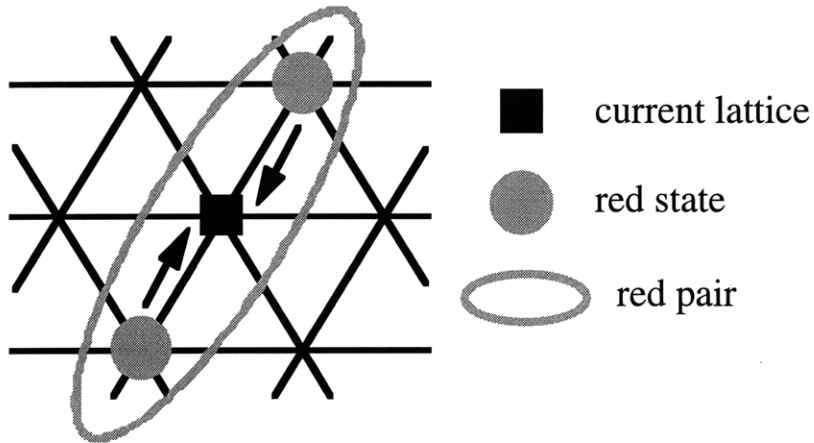


Figure 5-15 Each lattice point is labeled as a red or blue state depending on which color dominates at the lattice point. When the same two color states sandwich the current state as shown below, a 'state pair' is defined. The figure below shows an example of a 'red pair'. Arrows indicate that the red density will most-likely approach the current lattice from both sides.

The first step can be implemented using the idea of a "color pair." Each nearest neighboring lattice point has a color state of either red or blue, assuming that the color of the majority is selected when the lattice point has mixed colors. When two neighboring lattice points facing the opposite direction have the same color state, it is called a color pair as illustrated in Figure 5-15. When the current lattice point has the mass of both colors, and there is at least one color pair of each color, there must be more than one interface approaching the current lattice point, as shown in Figure 5-16. The information regarding the continuous phase at each lattice can be stored in memory. To calculate the correct color

gradient, the sign of c_i is inverted for one side of the non-continuous color state neighbors in Figure 5-16.

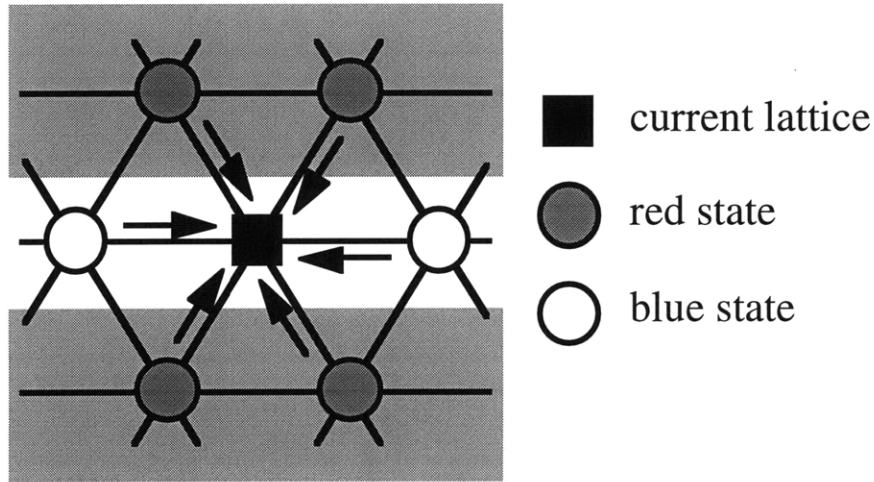


Figure 5-16 Existence of more than one each of red and blue pairs with respect to the current lattice indicates two (or unlikely, but more than three) interfaces are approaching the current state. When this condition occurs, use of some modified code that handles the interface recognition and color separation correctly is suggested.

Assuming the two interfaces are in parallel, the thickness of the continuous phase is calculated simply as the ratio of continuous phase to the entire density. When the thickness is above the critical value, the non-continuous phase is re-distributed in the order of directions that have the largest $|\vec{f} \cdot \vec{c}_i|$ values to the ones that have the smallest values. Two interfaces are preserved by this method. When the thickness drops below the pre-determined critical value, the standard color gradient defined by equation (4-3) and the standard color separation scheme are used. This results in the rupture a film of the continuous phase (coalescence).

In 3D FCHC lattice-Boltzmann method, a lattice site is connected to 18 neighboring lattice sites. Assuming two interfaces approach from z and $-z$ directions as shown in Figure 5-17, then there are only 10 lattice directions non-continuous phase (red) can flow after redistribution of colors. Therefore, when color ratio of the red at the current lattice site (black square) exceeds a half, there is a chance that some of reds flow into other 8 lattice directions. Since non-continuous phase flowing into the current blue lattice directions results in immediate breaking of the thin film, the above-described redistribution scheme can reduce the critical thickness only to about 0.5 lattice unit, unfortunately.

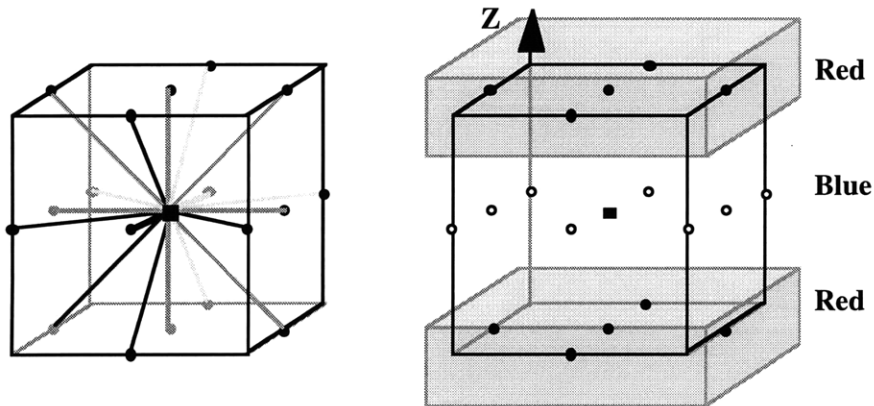


Figure 5-17 When two interfaces approach from z and $-z$ directions, there are only 10 lattice directions non-continuous phase (red) can flow after redistribution of colors. Therefore, when color ratio of the red at the current lattice site (black square) exceeds a half, there is a chance that some of reds flow into other 8 lattice directions.

Using this modification, the author conducted the same doublet collision simulations. Figure 5-18 compares the unmodified simulation and the modified simulation. Some delay in coalescence is observed because the new simulation program acknowledges two phase boundaries approaching each other.

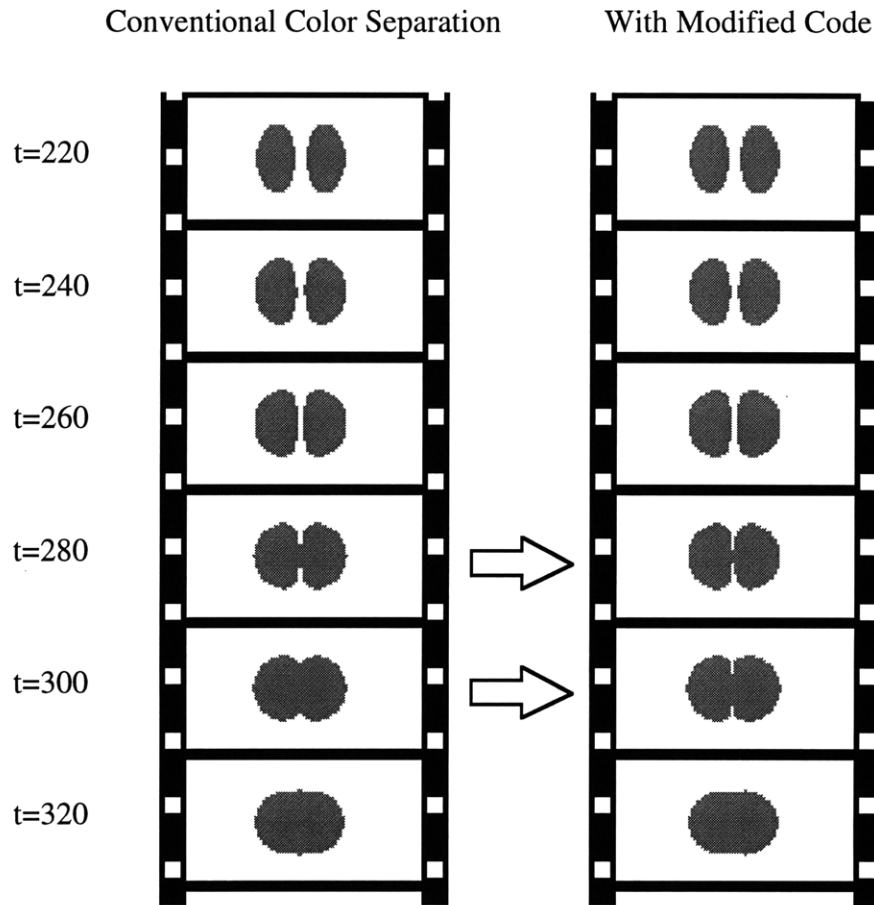


Figure 5-18 The delay in coalescence due to modification of the lattice-Boltzmann phase separation code relative to the conventional code is exhibited in the figure.

A dozen more simulations of doublet collision were conducted with the modified lattice-Boltzmann code. Although the coalescence was delayed to some extent, all still coalesced. The author concludes that this fundamental discrepancy was the result of limitations of the lattice and droplet size and the moving velocity of the doublet. Further improvements in the method of dealing with the phase boundary are required in order to correctly simulate the coalescence phenomena using the lattice-Boltzmann method.

5.5 Effect of Coalescence in Equilibrium Mixing

Droplet coalescence in mixing has a significant influence on the phase domain size distribution which is measured. The higher the concentration of the dispersed phase, the more frequently coalescence can occur. If the frequency of coalescence increases, the average droplet diameter at any given time should also increase.

Sundararaj and Macosko [54] experimented with the relationship between the droplet phase concentration and the droplet diameter, and confirmed this hypothesis. In their experiments, a batch mixer and two types of twin screw extruders were used for blending. At a given concentration of the droplet phase, the materials were mixed until the rate of breakup and coalescence reached equilibrium, then the average droplet diameter was measured using SEM.

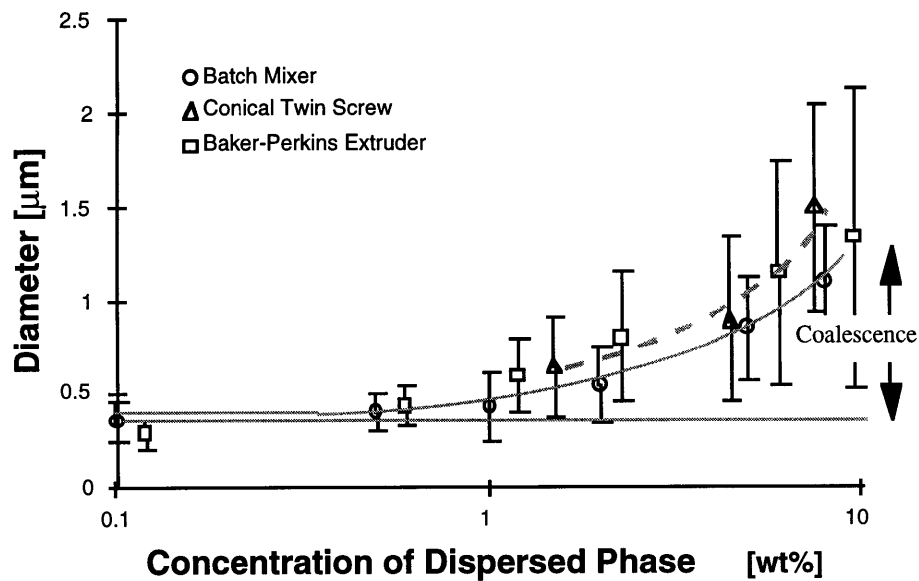


Figure 5-19 Sundararaj and Macosko's [54] experimental measurements of the average number diameters of droplets plotted against log of the concentration of dispersed phase. The diameters of droplets are measured at equilibrium of mixing.

They experimented with dispersed phase concentrations of between 0.1 to 10 percent. In most experiments, a visible increase in droplet diameter was observed starting at around 1% concentration as shown in Figure 5-19. The average diameter of the droplets observed at 10% concentration is two to three times larger than that at 1% concentration due to the effect of coalescence.

A simple shear flow was used in the lattice-Boltzmann method to qualitatively simulate the effect of coalescence in mixing at the macroscopic level. In the simulation, a 200x20x42 lattice was used. The interfacial tension was set so that the critical radius is around 2. After a single-phase flow reached equilibrium, droplets of radius 2 lattice unit were added randomly to increase the droplet phase concentration. The fluid was mixed in simple shear flow until equilibrium is reached. Once sheared equilibrium was reached, the number of droplets was counted, then counted again every 1000 timesteps for a total of four measurements. From the number of droplets and the given mass and density of droplet phase, the average radius was calculated at each time interval at each droplet phase concentration. Figure 5-20 shows typical states of equilibrium of mixing simulated by the lattice-Boltzmann method at different dispersed phase concentrations. Figure 5-21 shows the plot number average radius of the dispersed droplet as a function of its concentration, measured from the simulation results. The droplet radius begins increasing due to coalescence at around 1% droplet-phase concentration. This result qualitatively agrees with Sandararaj and Macosko's experimental results.

dispersed phase
concentration (wt%)

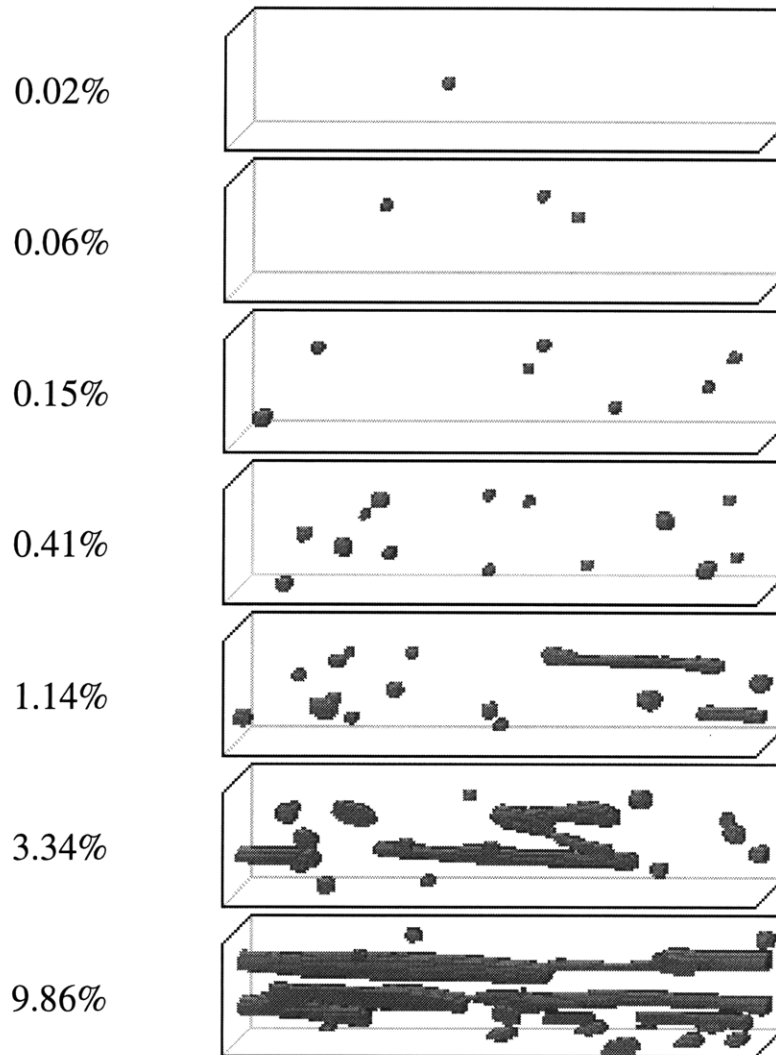


Figure 5-20 Typical states of equilibrium of mixing simulated by the lattice-Boltzmann method at different dispersed phase concentrations.

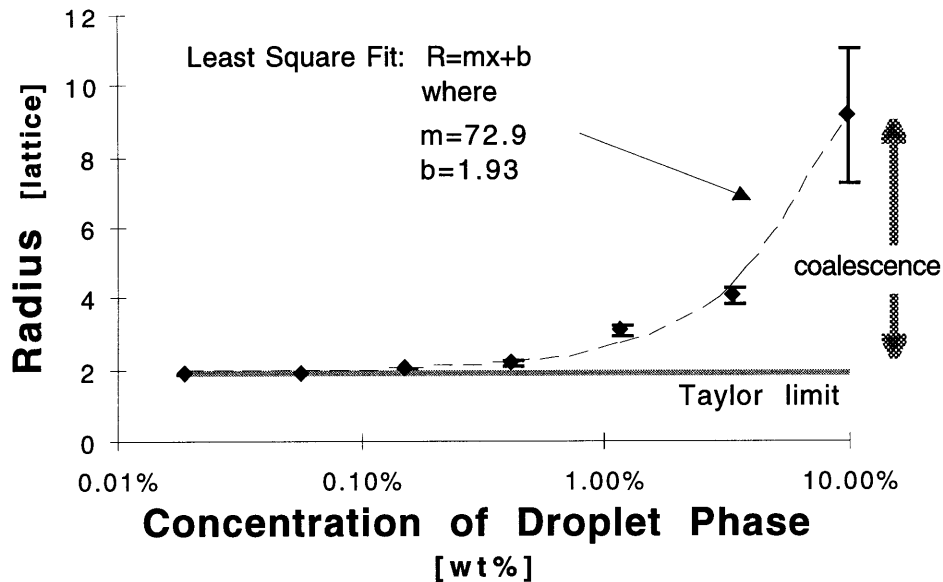


Figure 5-21 The lattice-Boltzmann simulation results are shown. Average number radius of droplets are plotted against the log of the concentration of the dispersed phase. Measurements are taken at equilibrium of mixing.

One should note that this simulation using simple shear flow significantly deviates from the complex flow situations produced in Sandararaj and Macosko's experiment. In simple shear with periodic boundary condition used in lattice-Boltzmann simulations, a droplet keeps traveling on a single path unless another droplet moving on a different, but parallel path coalesces with it. This simulation setup will affect the collision probability of the droplets. The probability of coalescence in the simulation also deviates from the real-life situation, as discussed in the previous doublet section. Further simulations using more true-to-life phase separation scheme and flow situations which truly model the complexity observed in batch-mixers or twin-screw extruders are required for semi-quantitative

comparison. Nevertheless, the macroscopic effect of coalescence in mixing at higher droplet phase concentrations is qualitatively confirmed in the lattice-Boltzmann simulations

6. Conclusion

The lattice-Boltzmann method was used for three-dimensional simulation of droplet breakup and coalescence in flow fields representative of those encountered in compounding of immiscible polymer blends.

First, the simulation method's capability in reproducing various hydrodynamic parameters such as the viscosity and the interfacial tension was verified. Using the single phase model, drag flow between parallel plates with one plate suddenly set in motion, and pressure flows of a Newtonian and a power-law fluids between parallel plates, were simulated. Using the two-phase model, a steady state sphere and a cylinder, and deformation of a droplet in simple shear were simulated. Within a range of kinematic viscosity which represent short mean free path with respect to the lattice size, quantitative accuracy of the simulation method was confirmed by comparing the simulation results with theory.

Capillary wave instability was simulated by applying the random perturbations in the simulation. Breakup of a cylindrical thread in a quiescent matrix was quantified in terms of the thread-breaking wavelength and the growth rate of the wave amplitude. The simulation results agreed with theory only in semi-quantitative sense. Causes for the deviations were investigated. Limitations of the simulation method rooted in its discrete spatial and time constraint were identified.

Droplet breakup in simple shear was simulated. Droplet shapes at the time of physical droplet breakup were compared with experimental results at different viscosity ratios and was shown qualitative agreements. The critical capillary number was

quantitatively measured at different viscosity ratios. The simulation results showed very good agreement with both experimental and theoretical results.

Phenomenon of end-pinching was simulated. As observed in experiment and suggested by vector analysis, the simulation method showed end-pinching when the ratio of droplet and matrix viscosities was small while it showed coalescence of two bulbous ends when the viscosity ratio was high.

Coalescence phenomena were simulated by head-on collision of a doublet in quiescent matrix and also by equilibrium of mixing at high-dispersed phase concentration in simple shear. Effects of coalescence were qualitatively observed in both simulations. However, the simulation method was observed to allow coalescence excessively in both cases. Errors associated with limitations in discrete lattice and color separation scheme were discussed.

The lattice-Boltzmann method showed significant potential in simulating complex flow situations such as high-dispersed phase concentrations, moving phase boundaries, and non-Newtonian rheology, which are essential in modeling polymer processing. While it quantitative showed its capability in simulating droplet breakup in simple shear, it still lacks quantitative accuracy in simulating coalescence phenomena. Droplet breakup in different flow geometries and further improvements for overcoming discrete effects in space and time, especially at phase domain boundaries, are required for its use in practical applications in the field of polymer processing.

7. Bibliography

- [1] S. Wu, *Polymer*, **26**, 1985, p.1855.
- [2] J. Hardy, Y. Pomeau, and O. de Pazzis, *J. Math. Phys.* **14**, 1973, p.1746.
- [3] S. Wolfram, *Theory and Application of Cellular Automata* (World Scientific, Singapore, 1986).
- [4] D. H. Rothman and Stéphane Zaleski, *Rev. Modern Phys.* **66**, No.4, 1994, p.1418.
- [5] U. Frisch, B. Hasslacher and Y. Pomeau, *Phys. Rev. Lett.* **56**, No.14, 1986, p.1505.
- [6] D. H. Rothman, *Lattice-gas Cellular Automata: Simple Models of Complex Hydrodynamics* (Cambridge Univ. Press, 1997).
- [7] A. K. Gunstensen, D. H. Rothman, S. Zaleski and G. Zanetti, *Phys. Rev. A*, **43**, No.8, 1991, p.4320.
- [8] D. H. Rothman, *Geophysics*, **53**, No.4, 1988, p.509.
- [9] D. H. Rothman and J. M. Keller, *J. Stat. Phys.*, **52**, No.3/4, 1988, p.1119.
- [10] C. Adler, D. d'Humières and D. H. Rothman, *J. Phys. I France*, **4**, 1994, p.29.
- [11] D. H. Rothman and S. Zaleski, *J. Phys. France*, **50**, 1989, p.2161
- [12] D. H. Rothman, *Phys. Rev. Lett.*, **65**, No.26, 1990, p.3305
- [13] M. Schelkle and A. Frohn, *J. Aerosol Sci.*, **24**, Supple.1, 1993, p.513.
- [14] A. K. Gunttensen And D. H. Rothman, *Physica D*, **47**, 1991, p.47.
- [15] B. M. Boghosian, P.V. Coveney and A.N. Emerton, *Proc. Roy. Soc. Lond. A*. **452**, 1996, p.1221.
- [16] G. R. McNamara and G. Zanetti, *Phys. Rev. Lett.*, **61**, No.20, 1988, p.2332.
- [17] A. K. Gunstensen and D. H. Rothman, *Europhys. Lett.*, **18**, No.2, 1992, p.157.
- [18] P. L. Bhatnagar, E. P. Gross and M. Krook, *Phys. Rev.* **94**, No.3, 1954, p.511.
- [19] D. d'Humières, P. Lallemand and U. Frisch, *Europhys. Lett.*, **2**, 1986, p.291.
- [20] I. Halliday and C. M Care, *Physical Review E.*, **53**, No.2, 1996, p.1602.
- [21] E. Aharonov and D. H. Rothman, *Geophys. Research Lett.*, **20**, No.8, 1993, p.679.
- [22] S. Hou, Q. Zou, G. Doolen and A. C. Cogley, *J Comp. Phys.*, **118**, 1995, p.329.
- [23] G. K. Batchelor, *An Introduction to Fluid Dynamics* (Cambridge Univ. Press, 1967), p.180, 191.
- [24] B. Szilágyi, R. Susan-Resiga and V. Sofonea, *Int'l J. Modern Phys. C*, **6**, No.3, 1995, p.345.
- [25] Z. Tadmor and C. G. Gogos, *Principles of Polymer Processing* (Wiley, 1979).
- [26] A. J. C. Ladd, *J. Fluid Mech.*, **271**, 1994, p.285.
- [27] I. Ginzbourg and P. M. Adler, *J. Phys. II France*, **4**, 1994, p191.
- [28] W. W. Graessley et al., *Trans. Soc. Rheol.*, **14**, 1970, p.519.
- [29] M. R. Swift, W. R. Osborn and J. M. Yeomans, *Phys. Rev. Lett.*, **75**, No.5, 1995, p.830.
- [30] G. I. Taylor, *Proc. R. Soc. London Ser. A*, **146**, 1934, p.201.
- [31] F. D. Rumscheidt and S. G. Mason, *J. Colloid Sci.*, **16**, 1961, p.238.
- [32] H. A. Stone, B. J. Bentley and L. G. Leal, *J. Fluid Mech.*, **173**, 1986, p.131.
- [33] J. Kang, T. G. Smith and D. I. Bigio, *AIChE J.*, **42**, No.3, 1996, p.649.
- [34] L. Rayleigh, *Proc. R. Soc. London*, **29**, 1879, p.71.
- [35] S. Tomotika, *Proc. R. Soc. London Ser. A*, **150**, 1935, p.322.

- [36] P. H. M. Elemans, J. M. H. Janssen and H. E. H. Meijer, *J. Rheol.*, **34**, No.8, 1990, p.1311.
- [37] S. H. Anastasiadis, I. Gancarz, and J. T. Koberstein, *Macromolecules*, **22**, 1989, p.1449.
- [38] J. J. Elemendorp and G. De Vos, *Polym. Eng. Sci.*, **26**, 1986, p.415.
- [39] R. J. Roe, *J. Colloid Interface Sci.*, **31**, 1969, p.228
- [40] D. Halliday and R. Resnick, *Physics I & II*, (Wiley, 1960) p.483.
- [41] D. W. van Krevelen, *Properties of Polymers: Correlations with Chemical Structure*, (Elsevier, 1972) p.150
- [42] J. M. H. Janssen, G. W. M. Peters and H. E. H. Meijer, *Chem. Eng. Sci.*, **48**, No.2, 1993, p.255.
- [43] H. A. Stone, *Annu. Rev. Fluid. Mech.*, **26**, No.65, 1994, p.102.
- [44] D. Barthés-Biesel and A. Acrivos, *J. Fluid Mech.*, **61**, 1973, p.1.
- [45] B. J. Bentley and L. G. Leal, *J. Fluid Mech.*, **167**, 1986, p.241.
- [46] H. P. Grace, *Chem. Eng. Commun.*, **14**, 1982, p.225.
- [47] H. A. Stone and L. G. Leal, *J. Fluid Mech.*, **198**, 1989, p.399.
- [48] G. F. Scheele and D. E. Leng, *Chem. Eng. Sci.*, **26**, 1971, p.1867.
- [49] W. Rommel, W. Meon and E. Blass, *Separation Sci. Tech.*, **27**, No.2, 1992, p.129.
- [50] D. Li, *J. Colloid Interface Sci.*, **181**, 1996, p.34.
- [51] S. A. K. Jeelani and S. Hartland, *Chem. Eng. Sci.*, **46**, 1991, p.1807.
- [52] D. Ramkrishna, *Rev. Chem. Eng.*, **3**, 1985, p.49.
- [53] R. Muralidhar and D. Ramkrishna, *6th Euro. Conf. Mixing*, 1988, p.213.
- [54] U. Sundararaj and C. W. Macosko, *Macromolecules*, **28**, 1995, p.2647.
- [55] J. F. Olson and D. H. Rothman, *J. Stat. Phys.*, **81**, No.1/2, 1995, p.199.
- [56] S. Torza, R. G. Cox, S. G. Mason, *J. Colloid Interface Sci.*, **38**, No.2, 1972, p.395.
- [57] G. D. M. MacKay and S. G. Mason, *Canadian J. Chem. Eng.*, **41**, 1963, p.203.